Sustainable Hydrogen Manufacturing via Renewable-Integrated Intensified Process for Refueling Stations

Akhil Arora,[a] Manali S. Zantye[a] and M. M. Faruque Hasan[a*]

[a] *Artie McFerrin Department of Chemical Engineering, Texas A&M University, College Station, TX 77843-3122, USA. Tel: (979) 862-1449; E-mail: hasan@tamu.edu*

Abstract

The widescale consumer adoption of hydrogen fuel cell electric vehicles (HFCEVs) is currently hindered by the high cost of small-scale hydrogen generation and the lack of extensive hydrogen fueling infrastructure. Natural gas-based hydrogen is cheaper when produced in large volumes but is also associated with high CO_2 emissions. To counter these challenges, we propose a hybrid approach where both natural gas and renewables are integrated in a synergistic manner using a dynamic process intensification technology that can be deployed onsite for meeting local demands of refueling stations. The technology is based on sorption enhanced steam methane reforming (SE-SMR) that utilizes a combination of reaction with *in-situ* CO_2 adsorption for enhancing process modularity, productivity and efficiency thereby outperforming conventional SMR at small scale. We develop a mixed integer linear programming (MILP)-based optimization framework for simultaneous design and scheduling of the SE-SMR process. The simultaneous optimization provides a synergistic combination whereby the renewables allow sustainable hydrogen manufacturing and the dynamic SE-SMR allows optimal use of the intermittency of the renewables. The U.S. nationwide analysis indicates that for futuristic renewable prices and a hydrogen production capacity of 2 ton/day, hydrogen can be produced at 50% less cost compared to the current cost of small-scale hydrogen generation. The city-wise analysis with varying hydrogen demand shows that even with just 5% HFCEV market

penetration level, hydrogen production cost less than $3/kg can be obtained at small scales across the United States with even cheaper hydrogen for large cities.
Keywords: Sustainable hydrogen, renewables, carbon capture, process simulation, process optimization

---

1. Introduction

The transportation sector contributes significantly to the overall anthropogenic carbon emissions. This sector needs to reduce its carbon emissions to achieve the goals set in the Paris agreement for climate change. More fundamental technological advancements are required to develop a more sustainable transportation sector [1]. In theory, reducing the energy intensity of vehicles by 50% and using alternate sustainable fuels such as hydrogen, fuel cells or electric batteries, can cut down the transport carbon emissions by 90-95% [1]. However, the transportation sector is currently the least diversified sector when compared to other energy end-use sectors, wherein more than 90% of the energy needs are powered by petroleum-based fuels [2]. To reduce transportation-related carbon emissions, there are active ongoing efforts to develop sustainable technologies and fuels [3, 4, 5]. Major efforts are focused on developing alternate fuels with lower carbon content or developing low-carbon transportation vehicles based on electric batteries or fuel cells [6, 7, 8].

Hydrogen is an energy carrier and a versatile feedstock with a wide range of applications in refining and petrochemicals, automotive and aerospace, power generation and transportation sectors. It has the highest energy content by weight among all existing fuels [9]. Hydrogen is crucial for transition to a low-carbon energy economy. In the transportation sector, there are several advantages of leveraging hydrogen as a fuel because of high octane number, wide flammability range, low ignition energy, low temperature, and short refueling time [10, 11]. A study by Colella et al [12] indicates that replacing fossil-fuel-on-road vehicles (FFOV) with hydrogen fuel cell electic vehicles (HFCEVs) sig-

nificantly reduces emissions. Even when compared to hybrid vehicles, HFCEVs achieve 14-23% reduction in emission based on whether the hydrogen is produced using natural gas or wind energy. Compared to electric cars with batteries, HFCEVs have much shorter refueling time, longer driving range and higher energy density [13].

By 2030, it is expected under ambitious hydrogen fuel deployment scenario, there will be up to 4300 large hydrogen refueling stations and 1500 material-handling refueling stations in the United States [14]. Furthermore, by 2050, the transportation sector is estimated to have the highest demand for hydrogen. There are several hydrogen-based transit fleet programs to increase consumer exposure to hydrogen-fueled vehicles and infrastructure[15]. Langford et al. [16] identified key requirements for transitioning to an entire hydrogen-based bus infrastructure with the help of Knoxville Area Transit system that predominantly relies on diesel bus fleets. In California, several large automakers such as Hyundai, Toyota and Honda commercially lease HFCEVs. The Government also invests to support the development of hydrogen infrastructure to aid in achieving California's air quality and carbon emission targets [17].

However, the major reasons preventing the widescale adoption of HFCEVs include the lack of extensive hydrogen refueling infrastructure, high hydrogen refueling costs, and low consumer awareness [18]. It is estimated that the price of hydrogen as a fuel will significantly impact the adoption of HFCEVs as it directly impacts the mileage costs [19]. Currently, hydrogen is predominantly produced in large-scale and centralized facilities using a combination of fossil, renewable and nuclear energy sources. Among the existing hydrogen production technologies, steam methane reforming (SMR) is the most economical thereby leading to its widespread prevalence for hydrogen generation [20]. Even though SMR-based hydrogen production from natural gas costs \$2-\$3/kg H_2, consumers have to pay as much as \$13-\$15/kg H_2 at refueling stations [21, 22]. This is due to the high hydrogen transportation and refueling station costs, which can approximately cost \$6-\$8/kg H_2 and \$7/kg H_2, respectively [19]. The cost of small-scale hydrogen generation alone currently ranges from \$5-6/kg H_2, which

is not economically viable. These costs are higher than the U.S. Department of Energy's cost target that includes the production and delivery costs [23].

The high hydrogen transportation cost can be effectively countered using small-scale and on-site hydrogen production plants that can cater to the hydrogen requirement of a single or multiple refueling stations. Small-scale on-site hydrogen generation has several economic and environmental advantages: lower cost and lower carbon emissions due to transportation avoidance, smaller capital investment, and decentralized nature of supply chains which prevents disruptions [16]. However, compared to large-scale SMR, small-scale hydrogen production technologies still suffer from diseconomies of scale. For instance, reducing the hydrogen production from 100 ton/day to 0.5 ton/day can increase the per-unit production cost by as much as 70% [24].

To counter the diseconomies of scaling prevalent in small-scale hydrogen manufacturing, we utilize a small-scale, modular and compact hydrogen production technology based on the concepts of Process Intensification (PI). PI aims at significantly reducing the energy intensity and cost, and improving the productivity and efficiency of chemical processes by exploring synergy between multiple phenomena at different time and spatial scales [25, 26, 27]. The specific PI technology leveraged here is called sorption enhanced reaction process (SERP), which combines an admixture of solid adsorbent and catalyst in an intensified column to simultaneously perform chemical conversion and byproduct removal [28, 29, 30, 31]. Fundamentally, the SERP technology is based on the Le Chatelier's principle which states that selective removal of reaction byproduct(s) can shift reaction towards the forward direction thereby leading to higher overall conversion. For hydrogen manufacturing, the specific SERP process we consider is called sorption enhanced steam methane reforming (SE-SMR). In SE-SMR, the reforming reactions are promoted through Ni-based catalyst and the carbon dioxide byproduct is selectively removed from the reaction gas mixture using hydrotalcite (HTC) chemisorbent. The resulting intensified process has higher single-pass conversion, product purity, lower operating temperature and enhanced heat integration compared to the traditional non-intensified SMR

process [32].

There already exists several literature studies on modeling and simulation of SE-SMR systems. Waldron et al [33] experimentally demonstrated a 4-step Skarstrom-type SE-SMR process for producing hydrogen with more than 90% purity at a much lower reaction temperature range of 450-550 °C compared to conventional SMR. Xiu et al [34] studied non-isothermal, non-isobaric and non-adiabatic nature of SE-SMR processes using a mathematical model. Their analysis indicated that hydrogen with 88% purity and traces of carbon dioxide and carbon monoxide could be produced. Johnsen et al [35] experimentally investigated a fluidized bed reactor for SE-SMR with dolomite as the carbon dioxide-acceptor. On a dry basis, more than 98% pure hydrogen could be manufactured. Li et al [36] developed an SE-SMR process with a calcium-based sorbent for removing carbon dioxide, and performed several carbonation/calcination cycles for investigating the longevity of the sorbent. There exist several additional works on SE-SMR the details for which can be found in comprehensive review papers elsewhere [37, 38, 39, 40].

Although there exists a significant amount of literature on hydrogen production via SE-SMR, a majority of the works focuses on either improving the materials used for removing carbon dioxide from SMR reaction gas mixture, or optimizing the cyclic operation of SE-SMR process. Moreover, most existing works are focused predominantly on improving single-pass methane conversion but do not consider the carbon capture and sequestration aspect for driving process sustainability. The objective of the current work is to develop a sustainable, low-carbon and efficient hydrogen production process and pathway while simultaneously capturing byproduct carbon dioxide to lower direct emissions. For lowering indirect carbon emissions due to electricity consumption, we incorporate renewable energy in the form of solar PV and wind turbine.

To investigate such a complex process scheme with dynamic interactions of renewable availability, electricity market, hydrogen demand and process dynamics, we develop a novel multi-scale computational framework that efficiently integrates and simultaneously solve for process design and scheduling decisions.

Through our analysis, we answer several important questions:

- What are the hydrogen cost benchmarks achievable through the proposed renewable-integrated SE-SMR process?
- Which renewable technology is more suitable for hydrogen manufacturing given spatiotemporal variation in consumer hydrogen demand, renewable availability and SE-SMR process dynamics?
- What is the effect of regional hydrogen demand on hydrogen production cost?
- What are the effects of varying renewable, natural gas and electricity prices on hydrogen production cost?
- What are the estimated hydrogen production costs under different HFCEV market penetration scenarios?

The computational framework is based on a large-scale mixed integer linear programming (MILP) model that minimizes hydrogen production cost while incorporating SE-SMR process design and operation constraints, power flow from grid and renewables to process equipment and process economics. For performing high-fidelity simulations of SE-SMR processes, a generalized reaction-adsorption modeling and simulation (GRAMS) platform is utilized [30]. To maintain the MILP nature of the problem, the complex non-linearities in SE-SMR process dynamics and cost correlations are adequately represented by artificial neural network (ANN)-based regression models. The MILP model is then utilized for performing several nationwide case studies to minimize hydrogen production cost with varying hydrogen demand and market maturity levels, renewable availability, and electricity prices.

The article is structured as follows. Section 2 describes the sustainable and intensified SE-SMR process, and its integration with renewable sources of energy. The section also highlights the key advantages offered by the renewable-integrated SE-SMR process compared to the conventional SMR process for hy-

drogen production. Section 3 presents the overall model developed for high-fidelity simulation and optimization of SE-SMR processes. Specifically, the section describes the first-principles simulation model, process performance metrics, and the MILP model that is utilized for simultaneous design and scheduling of the renewable-integrated SE-SMR process. Section 4 depicts the regional and nationwide case studies to answer the questions regarding the effect of hydrogen production capacity scale, HFCEV market maturity, renewable availability, electricity and natural gas prices on hydrogen production costs. The analysis presented is vital for evaluating the cost-effectiveness of the proposed hydrogen production pathway for meeting hydrogen fuel cost targets.

2. Renewable-Integrated Hydrogen Production Process

To ensure the sustainability of the SE-SMR process, we utilize renewable-generated electricity for powering the energy requirement of reforming reactions, and sequester the byproduct carbon dioxide after utilizing a sequence of compression and cooling stages. As the hydrogen is derived from natural gas with carbon sequestration, the resulting hydrogen produced is termed as *blue hydrogen* [41]. The electrification of the SE-SMR process is especially possible due to the integration of PI to the conventional SMR process. This results in lower temperature requirement for facilitating reforming reactions, which can be more readily achieved through electric heating. In addition, replacing a furnace typically employed in SMR process with electric heating significantly reduces process scale, carbon emissions and waste streams.

Wismann et al [42] recently utilized a similar concept for developing a sustainable and efficient SMR process with the use of direct resistive/ohmic heating powered by renewable electricity. In their reactor design, renewable electricity was utilized for directly heating the catalytic structure thereby establishing an intimate contact between the heat source (i.e., catalyst structure) and the reaction gas mixture. This drove the reaction closer to equilibrium as there were no significant temperature gradients within the reactor column. There also ex-

ists literature studies that directly or indirectly utilize renewables for fueling the energy requirements of other endothermic reforming reactions that require high temperature. Rieks et al [43] experimentally demonstrated an electrically heated reformer for dry reforming of methane to produce synthesis gas from carbon dioxide feed. Dahl et al [44] used concentrated solar power for methane dry reforming wherein they directly utilized solar energy in the reactor to achieve high reaction temperatures. Several other studies also investigate storing renewable power through renewable-driven reforming reactors that differ in reactor or process designs and performance characteristics [45, 46, 47, 48].

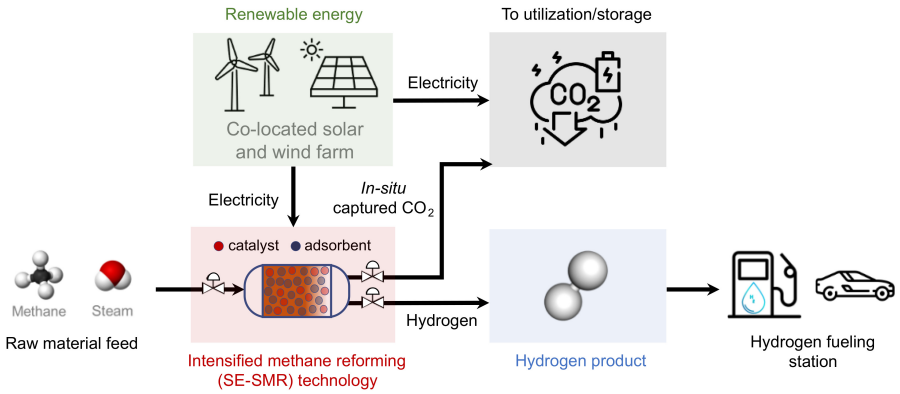

Figure 1: Proposed renewable-integrated and intensified production pathway for sustainable manufacturing of blue hydrogen with *in-situ* carbon capture for meeting localized hydrogen refueling station demands. The proposed technology utilizes steam and methane as the feedstock to manufacture hydrogen via intensified steam methane reforming.

The proposed renewable-integrated distributed and intensified production pathway for manufacturing blue hydrogen from methane is shown in Figure 1. The raw material/feedstock consists of a mixture of methane and steam, which reacts in the SE-SMR reactor module to produce hydrogen product. The hydrogen manufactured is utilized for fulfilling the demand of refueling stations. The SE-SMR process is especially suited for sustainable hydrogen production due to higher single-pass reaction conversion, lower operating temperature, and

production of high purity hydrogen thereby eliminating the need of additional purification stages. As a byproduct of the reforming reactions, carbon dioxide is also formed that is compressed to a high pressure for sequestration purposes. The SE-SMR reactor is electrified and the heating requirements are met through the electricity produced from renewables and grid. In addition, renewable energy is utilized for steam generation via electric boiler, compression and heating purposes. Due to intermittent nature of renewable availability, a combination of electricity from co-located renewable farm and grid is required to satisfy process energy requirements throughout a day.

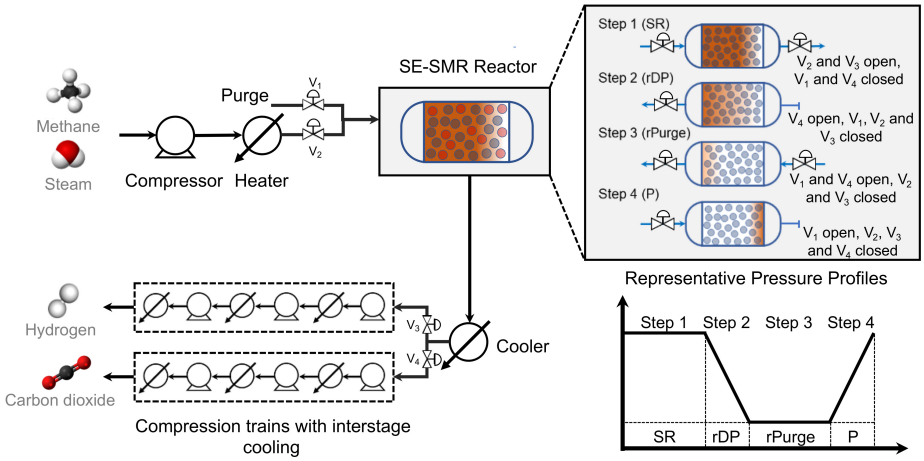

Figure 2: SE-SMR process including auxiliary equipment for producing hydrogen from steam and methane feed mixture.

Figure 2 depicts the overall SE-SMR process in more detail. Here, the incoming steam and methane gas mixture is firstly compressed and heated. Once their temperature and pressure reach the desired reactor operating conditions, the mixture is sent to the SE-SMR reactor which is packed with an admixture of Ni-Al catalyst and carbon dioxide-selective HTC adsorbent. The Ni-Al catalyst facilitates the following reforming reactions, whereas the HTC adsorbent selectively removes carbon dioxide from the reaction gas mixture to push reaction

equilibrium in the forward direction.

$$\mathrm{CH_4(g) + H_2O(g) \rightleftharpoons CO(g) + 3\,H_2(g)}, \Delta H_{r,I} = 206.1 \text{ kJ/mol} \quad \text{(I)}$$

$$\mathrm{CH_4(g) + 2\,H_2O(g) \rightleftharpoons CO_2(g) + 4\,H_2(g)}, \Delta H_{r,II} = 164.9 \text{ kJ/mol} \quad \text{(II)}$$

$$\mathrm{CO(g) + H_2O(g) \rightleftharpoons CO_2(g) + H_2(g)}, \Delta H_{r,III} = -41.2 \text{ kJ/mol} \quad \text{(III)}$$

Due to limited adsorption capacity of HTC adsorbent, the SE-SMR reactor undergoes a Skarstrom-type cyclic operation with periodic switching between hydrogen production and adsorbent regeneration steps. Specifically, the SE-SMR cycle considered consists of a sequence of 4 steps which are repeated periodically. The cycle includes (i) sorption-reaction (SR), (ii) reverse depressurization (rDP), (iii) reverse purge (rPurge) and (iv) pressurization (P) steps. During the SR step, the methane and steam mixture is sent to the SE-SMR reactor at high pressure for hydrogen production. The high purity hydrogen product is then sent to the multi-stage compression train for storage purposes. Once the adsorption saturation capacity of HTC is reached, the inlet methane and steam flow is cut off, and the SE-SMR column pressure is decreased to atmospheric pressure during rDP step. For purging out the adsorbed carbon dioxide during the rPurge step, a mixture of 95% steam and 5% hydrogen is utilized [49]. The carbon dioxide purged during the rPurge step is separated and sent through the multi-stage compression train for storage and utilization purposes. Finally, pure steam is used during the P step for pressurizing the column back to the required pressure during SR step.

Due to the dynamic and multi-step nature of the SE-SMR cycle, the average stepwise energy requirement of different equipment varies. For most of the cycle duration, the SE-SMR column is either in the SR step or in the rPurge step since the rDP and P transition steps are much shorter than the SR and rPurge steps. Due to high steam flow rate requirement for column purging, the overall energy requirement during the rPurge step is higher compared to the SR step. This results in an alternating sequence between the low and high power demand phases during a multi-cycle operation. For achieving a close to steady-state power requirement, we consider the design and scheduling of two SE-SMR

modules that are operated simultaneously. We further assume that the SR and rPurge steps have equal durations, rDP and P steps are 20 s long, and one of the modules is operated with an offset of half cycle time. Consequently, when one module is undergoing the SR step for hydrogen production, the other module is regenerated during rPurge step due to the offset of half cycle time. Using this synchronous operation of two modules, we ensure that there is minimum fluctuation of power requirement along the scheduling horizon. The effects of using this strategy on stabilizing power requirement can be observed later in the results section.

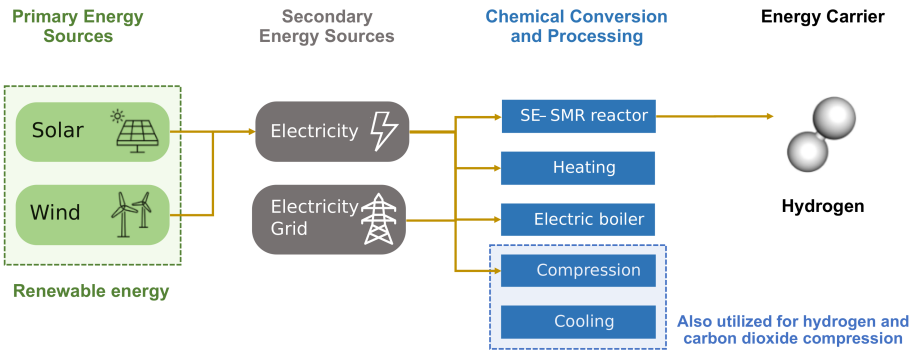

Figure 3: Power flow from primary and secondary energy sources to energy sinks that include SE-SMR and auxiliary process equipment. Specifically, the primary energy sources are solar PV and wind turbine that generate renewable electricity which, when combined with electricity sourced from grid, is used to power the energy demands of several unit operations which include intensified reactors, heaters, electric boilers and compressors.

The power flow from energy sources to sinks are shown in Figure 3. Since the SE-SMR process is electrified, the major utility that powers the entire process is electricity along with cooling water that is utilized for cooling hydrogen and carbon dioxide outlet streams. Solar PV and wind turbine constitute the primary sources of energy that are utilized for generating renewable electricity, which when combined with electricity sourced from grid is used to power the energy demands of process unit operations. Specifically, electricity is utilized to satisfy energy requirements of SE-SMR reactors, heaters, coolers, and electric

boilers. The major decision is, therefore, to have an optimal mix of electricity coming from renewable sources and grid to reduce the hydrogen production cost while maintaining the sustainability of the process.

3. Model Development

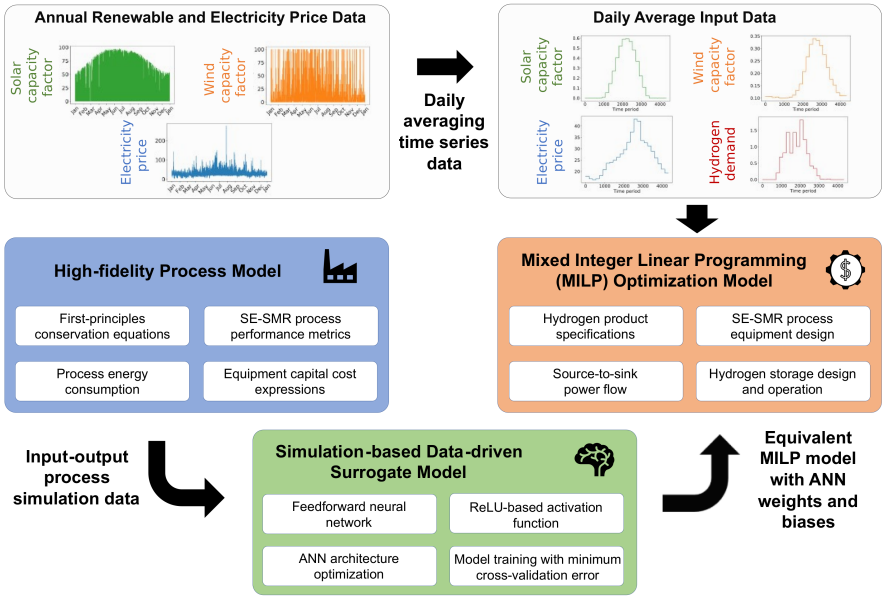

Figure 4: Overall computational framework for simultaneous design and operation of SE-SMR process with minimum hydrogen production cost.

The overall computational framework developed for minimizing hydrogen production cost is shown in Figure 4. There are several steps that are followed to ensure the computational tractability of the large-scale SE-SMR design and scheduling problem. The core of the framework is based on a MILP model that minimizes hydrogen production cost while satisfying several sets of constraints on hydrogen production specifications, equipment design, and power flow from energy sources to sinks, among others. Daily average input data representing the dynamic variations in solar/wind availability and electricity prices are also considered. These are typically obtained from annually reported data [50]. To capture the nonlinear dynamics of SE-SMR processes, we develop

an ANN-based input-output model that maps the output process performance metrics and equipment capital costs to input design and operational decisions. The ANN model utilizes a first-principles high-fidelity simulation model that represents the integrated reaction and adsorption phenomena occurring inside SE-SMR column. This section presents these constituting elements of the overall framework in more detail.

3.1. Renewable Availability Model

As the renewable sources are available intermittently, the power generated is less than the maximum design capacity. Therefore, to consider the renewable intermittency, the capacity factors for solar PV and wind turbines are calculated as follows. The capacity factors denote the utilization of renewable sources as, for a given renewable technology, the actual power output is obtained by multiplying capacity factor with corresponding design capacity.

The following equation is used for obtaining the capacity factor for solar PV (cf_t^{solar}) at time t:

$$cf_t^{solar} = \frac{H_t}{H^{ref}} \eta^{arr} \eta^{dc/ac} \eta^{wir}, \tag{1a}$$

where, H_t is the solar irradiance at time t, and $H^{ref} = 1000$ W/m^2 is the reference solar irradiance. η^{arr}, $\eta^{dc/ac}$ and η^{wir} are respectively the efficiencies for solar PV array, DC to AC conversion and wiring, and the product of these efficiencies equals 93.75% [50].

For computing time-varying wind capacity factor cf_t^{wind}, the following power law curve is used [51]:

$$cf_t^{wind} = \begin{cases} 0, & v_t^{wind} \leq v^{ci,w} \\ \dfrac{{v_t^{wind}}^3 - {v^{ci,w}}^3}{{v^{r,w}}^3 - {v^{ci,w}}^3}, & v^{ci,w} \leq v_t^{wind} \leq v^{r,w}, \\ 1, & v^{r,w} \leq v_t^{wind} \leq v^{co,w}, \\ 0, & v_t^{wind} \geq v^{co,w}, \end{cases} \tag{1b}$$

where, $v^{ci,w} = 1.5$ m/s is the cut-in wind speed, $v^{r,w} = 12$ m/s is the rated wind speed, and $v^{co,w} = 25$ m/s is the cut-off wind speed [50]. Below the cut-in

wind speed and above the cut-off wind speed, the wind turbine does not produce any power. At high wind speeds above cut-off speed, the rotor is stopped to prevent any damage to the wind turbine. Between the cut-in and rated speed, output power is a cubic function of wind speed. When the wind speed is between rated and cut-off speeds, the output power is maximum and is equal to the rated power. v_t^{wind} is the adjusted wind speed at time t at a typical wind turbine hub height of 80 m [52]. It is computed using the following 1/7 power law expression:

$$v_t^{wind} = v_t^{wind,i} \left(\frac{80}{10}\right)^{\frac{1}{7}}, \tag{1c}$$

where, wind speed $v_t^{wind,i}$ is obtained from the NREL's database measured at a height of 10 m [53].

3.2. High-fidelity Process Model

The model utilized for performing high-fidelity simulations of the SE-SMR process is based on a one-dimensional, pseudo-homogeneous, non-adiabatic, non-isothermal and non-isobaric model [30, 31, 54]. The first-principles model consists of a set of nonlinear and algebraic partial differential equations (NAPDEs) which represent the conservation of mass, momentum and energy. By solving the NAPDE model, the spatiotemporal variations in chemical species concentration, temperature and pressure are obtained.

The first-principles conservation equations utilized in the model are reported in Section S1 in the Supplementary Data. Specifically, the equations consist of component and total mass balance, heat balance, steady-state momentum balance and gas-to-solid transfer of adsorbate species. These equations are solved simultaneously to compute several process performance metrics that include produced hydrogen purity and productivity. The details of these metrics are reported in Section S1 in the Supplementary Data. These constitute the overall NAPDE model that represents the hybrid reaction-adsorption phenomena occurring within SE-SMR column. The dimensional equations are appropriately scaled to result in a dimensionless NAPDE model. Subsequently, the finite

volume method is utilized with the upwind difference scheme to discretize the partial differential equations in the spatial dimension. To solve the resulting set of ordinary differential equations, we leverage the ode15s solver in MATLAB. More information regarding the dimensionless equations, system boundary conditions, discretization scheme and solution strategy can be found in Arora et al [30].

In addition to the first-principles equations, we utilize several additional expressions to compute the energy consumption for different equipment in the SE-SMR process. These include the expressions for computing compressor work, heater and cooler duty, and amount of heat provided to SE-SMR reactor. These equations are reported in Section S2 in the Supplementary Data. Moreover, the capital cost of the overall process consists of total installed costs of SE-SMR process equipment, and costs of solar PV, wind turbine, electric boiler and hydrogen storage tank. The capital cost expressions for these equipment are reported in Section S3 in the Supplementary Data.

3.3. ANN-based Discretely Linear Surrogate Model

The high-fidelity process model consists of a complex NAPDE model which prevents its direct application for optimization studies. In addition, the equipment cost expressions have inherent non-linearities and non-convexities. To simplify their incorporation in the overall optimization model, we develop and train SE-SMR process and cost ANN models. Using them, a set of equivalent MILP constraints are then incorporated in the overall optimization problem that represent the calculations occurring within cost and process ANN models. Both ANN models have the same form and are utilized for computing equipment costs and process dynamics in the two SE-SMR modules. Within the ANN architecture, we leverage feedforward neural networks with rectified linear unit (ReLU)-based activation function, which are eventually converted to equivalent low-complexity MILP models [55, 56, 57]. This is especially advantageous in retaining the MILP nature of the broader hydrogen cost minimization problem, and in efficiently solving the large-scale integrated process design and scheduling

model. There are other activation functions (e.g., sigmoid, tanh, logistic) which result in equivalent nonlinear programming (NLP) formulations. However, we select the ReLU activation function due to its MILP nature, faster convergence, and better generalization capabilities [58, 59]. The equivalent MILP constraints that represent the computations occurring within ANN are reported in Section S5 in the Supplementary Data.

During ANN model development for SE-SMR process representation, the input data consists of process design and operational decisions whereas the output data consists of hydrogen product specifications, equipment energy consumption and carbon dioxide capture rate. In case of approximating nonlinear cost expressions via MILP-based ANN surrogate models, the input data consists of equipment design and operational variables, and the output data consists of equipment cost values. Using the input data vector, the MILP-based ANN equations compute the output data values. As a result of replacing SE-SMR process and cost expressions, we can formulate the overall optimization problem as an MILP problem. If the MILP-based ANN models are not incorporated, we would need to utilize original expressions (e.g., nonlinear cost expressions in Section S3) which would thereby require solving a more complex MINLP class of problems. Therefore, converting the non-linearities in SE-SMR process and cost correlations to equivalent MILP expressions are crucial in maintaining the computational tractability of the resulting optimization problem.

For both SE-SMR process and cost ANN models, the input and output variables and the respective lower and upper bounds are reported in Tables S4-S5 in the Supplementary Data. For generating input-output data for model training, the Latin Hypercube sampling method is utilized for generating 10000 input data points, and simulations are then performed to obtain the corresponding output data. For model training, the Adam algorithm is utilized through the Keras deep learning in python environment, and the objective during model training is to minimize the mean square loss [60, 61]. Separate input-output datasets with 5000 samples are generated for cross-validating the trained ANN models. For hyperparameter optimization, the model training and cross-

validation steps are performed for different ANN model size. Specifically, we fix the number of hidden layers to be one and vary the number of nodes within the hidden layer. For each of the ANN models, the training and cross-validation accuracies are reported in Table S6 in the Supplementary Data. The ANN models with 50 nodes in the hidden layer are selected for representing the SE-SMR process dynamics and process equipment costs as they have the highest cross-validation accuracy.

3.4. MILP Optimization Model

The overall optimization problem is stated as follows. Given the spatiotemporal variability in data for renewable availability, electricity price and consumer hydrogen demand, design and schedule the overall SE-SMR process with two synchronized modules such that the overall hydrogen production cost is minimized while meeting the constraints on hydrogen product specifications, equipment design, source-to-sink power flow and hydrogen storage tank. While solving this problem, the major design and process operation decisions include optimally sizing the reactor modules (i.e., number of tubes, bed length), determining the optimal process operating conditions (i.e., reactor pressure, feed velocity, steps duration), computing the optimal size of auxiliary equipment such as compressors, coolers, heaters and electric boilers, and sizing the renewable sources. In addition, the major scheduling decisions that need to be optimized include obtaining the optimal power flow schedule from energy sources to energy sinks, and the hydrogen production and storage schedule.

Let us consider that the set $\mathcal{T}$ represents the scheduling time horizon where $t \in \mathcal{T} = \{1, 2, ..., NT\}$, and NT is the number of discrete time intervals. The SE-SMR cyclic steps are included in the set $\mathcal{S}$ and the index $s \in \mathcal{S} = \{SR, rDP, rPurge, P\}$ represents each of the periodic cycle steps. The set $\mathcal{M}$ consists of the two SE-SMR modules, and $m \in \mathcal{M} = \{1, 2\}$. For defining process design and operating variables, a master set $\mathcal{D}$ is defined which consists of SE-SMR reactor design and operating variables, as well as other auxiliary equipment. Therefore, $d \in \mathcal{D} = \{P^f, v^f, v^{purge}, \alpha^{ad/cat}, L, n^{tubes}, fc, fh, oc, reac, cc1,$

$cl1, cc2, cl2, cc3, cl3, hc1, hl1, hc2, hl2, hc3, hl3\}$.

Here, P^f and v^f are respectively the steam and methane feed pressure and superficial velocity, v^{purge} is the purge feed superficial velocity, $\alpha^{ad/cat}$ is the adsorbent to catalyst ratio in the SE-SMR column, L is the column length, and n^{tubes} is the number of tubes in an SE-SMR module. fc, fh and oc are respectively feed compressor, feed heater and outlet cooler, $reac$ denotes the SE-SMR reactor, $cc1, cc2$ and $cc3$ are the three compressors in CO_2 multistage compression train, $cl1, cl2$ and $cl3$ are the three interstage coolers, and H_2 multistage compressors and coolers are denoted by $hc1, hc2, hc3$ and $hl1, hl2, hl3$, respectively. Moreover, a set $\mathcal{R}$ consisting of energy sources is defined where $r \in \mathcal{R} = \{solar, wind, grid\}$. The sets $\mathcal{N}_1^{in}$ and $\mathcal{N}_2^{in}$ contain the inputs to the two ANN models for representing SE-SMR process dynamics and cost expressions, respectively, such that $n_1^{in} \in \mathcal{N}_1^{in} = \{1, 2, ..., 8\}$ and $n_2^{in} \in \mathcal{N}_2^{in} = \{1, 2, ..., 20\}$. Additionally, the sets $\mathcal{N}_1^{out}$ and $\mathcal{N}_2^{out}$ consist of the outputs of the two ANN models, and $n_1^{out} \in \mathcal{N}_1^{out} = \{1, 2, ..., 30\}$ and $n_2^{out} \in \mathcal{N}_2^{out} = \{1, 2, ..., 15\}$.

The following three subsets are defined over $\mathcal{D}$: $e \in E_d = \{fc, fh, oc, reac, cc1, cl1, cc2, cl2, cc3, cl3, hc1, hl1, hc2, hl2, hc3, hl3\}$ is the subset containing SE-SMR process equipment, $e \in EP_d = \{fc, fh, reac, cc1, cc2, cc3, hc1, hc2, hc3\}$ consists of the equipment that require electricity for meeting energy demands, and $e \in C_d = \{oc, cl1, cl2, cl3, hl1, hl2, hl3\}$ comprises of equipment that require cooling water utility. In addition, a subset $Ren_r = \{solar, wind\}$ consisting of renewable energy sources is defined.

Using the aforementioned set definitions, the following set mappings are defined: $map^p_{e,s,n_1^{out}}$ denotes whether process equipment e requires energy during step s and the process ANN output n_1^{out} that provides the corresponding amount of energy required, $map^{pc}_{n_1^{in},n_2^{in}}$ connects some of the inputs of the process and cost ANN models, $map^{c1}_{d,n_2^{in}}$ links the design d to the input of cost ANN model n_2^{in}, and $map^{c2}_{e,n_2^{out}}$ is utilized for mapping equipment e to its corresponding cost ANN output n_2^{out}. The elements defined in these set mappings are reported in Table S1 in the Supplementary Data.

Additionally, we define several model parameters and decision variables. Table S2 in the Supplementary Data reports all of the parameters required in the optimization model, which majorly consist of time-varying solar and wind capacity factors, hydrogen product demand, cost parameters for different SE-SMR equipment and raw material feedstock, equipment efficiency, and chemical species' properties. A majority of the parameters have fixed values, whereas other parameter values are dependent on geographical location, hydrogen production capacity, or the specific optimization scenario that is performed. In addition to these input parameters, the comprehensive list of decision variables that need to be optimized are reported in Table S3 in the Supplementary Data.

The MILP model developed for minimizing hydrogen production cost is as follows. The objective of the MILP model is to simultaneously optimize numerous design, operational and scheduling decisions while considering the time

horizon of one representative day with 4320 discrete time periods.

$$\min \quad C^{\mathrm{H_2}} = \frac{\phi^{cap,d} \cdot TIC^T + OC^T}{PD^{min}}, \tag{2a}$$

$$\text{s.t.} \quad Pur_m^{\mathrm{H_2}} \geq P^{\mathrm{H_2},min}, \ \forall m \in \mathcal{M}, \tag{2b}$$

$$PD^{\mathrm{H_2},total} \geq PD^{min}, \tag{2c}$$

$$PD^{\mathrm{H_2},total} = \frac{\left(\sum_{m\in\mathcal{M}} PD_m^{\mathrm{H_2}}\right) NT}{t^{cycle}}, \tag{2d}$$

$$PD_{m,t}^{\mathrm{H_2},tp} = \frac{PD_m^{\mathrm{H_2}} \cdot z_{m,t,SR}}{t_{SR}^{step}}, \ \forall m \in \mathcal{M}, t \in \mathcal{T}, \tag{2e}$$

$$TIC^T = \sum_{m\in\mathcal{M}} \sum_{e\in E_d} TIC_{m,e}^{PE} + TIC^R + TIC^B + TIC^{\mathrm{H_2}}, \tag{2f}$$

$$OC^T = OC^{\mathrm{CH_4}} + OC^C + OC^E - Rev^{\mathrm{CO_2}}, \tag{2g}$$

$$TIC_{m,e}^{PE} = y_{m,n_2^{out}}^{a2}, \ \forall m \in \mathcal{M}, \forall (e, n_2^{out}) \in map_{e,n_2^{out}}^{c2}, \tag{2h}$$

$$TIC_{m,fh}^{PE} = D_{m,fh} \cdot c^{fh}, \ \forall m \in \mathcal{M}, \tag{2i}$$

$$TIC^R = c^{solar} \cdot D_{solar}^R + c^{wind} \cdot D_{wind}^R, \tag{2j}$$

$$TIC^B = \sum_{m\in\mathcal{M}} D_m^B \cdot c^B, \tag{2k}$$

$$TIC^{\mathrm{H_2}} = D^{\mathrm{H_2}} \cdot c^{\mathrm{H_2},store}, \tag{2l}$$

$$OC^{\mathrm{CH_4}} = \left(\sum_{m\in\mathcal{M}} \sum_{t\in\mathcal{T}} R_{m,t}^{\mathrm{CH_4}}\right) \Delta t \cdot MW^{\mathrm{CH_4}} \cdot P^{\mathrm{CH_4}}, \tag{2m}$$

$$OC^C = \left(\sum_{m\in\mathcal{M}} \sum_{e\in C_d} \sum_{t\in\mathcal{T}} E_{m,e,t}^{dem}\right) \frac{\Delta t \cdot P^{\mathrm{H_2O}}}{Cp^{\mathrm{H_2O}} \cdot \Delta T^{\mathrm{H_2O}}}, \tag{2n}$$

$$OC^E = \left(\sum_{m\in\mathcal{M}} \sum_{e\in EP_d} \sum_{t\in\mathcal{T}} P^{flow}_{grid,m,e,t} \cdot EP_t + \sum_{m\in\mathcal{M}} \sum_{t\in\mathcal{T}} PB^{flow}_{grid,m,t} \cdot EP_t \right) \frac{\Delta t}{3.6\times 10^6}, \tag{2o}$$

$$Rev^{\mathrm{CO_2}} = \left(\sum_{m\in\mathcal{M}} \sum_{t\in\mathcal{T}} E^{\mathrm{CO_2}}_{m,t} \right) \Delta t \cdot MW^{\mathrm{CO_2}} \cdot (P^{\mathrm{CO_2}} - TS^{\mathrm{CO_2}}), \tag{2p}$$

$$\sum_{r\in\mathcal{R}} P^{flow}_{r,m,e,t} \cdot \eta^{ss}_{r,e} = E^{dem}_{m,e,t},\ \forall m \in \mathcal{M}, \forall e \in EP_d, \forall t \in \mathcal{T}, \tag{2q}$$

$$\sum_{m\in\mathcal{M}} \sum_{e\in EP_d} P^{flow}_{solar,m,e,t} + \sum_{m\in\mathcal{M}} PB^{flow}_{solar,m,t} \le cf^{solar}_t \cdot D^R_{solar},\ \forall t \in \mathcal{T}, \tag{2r}$$

$$\sum_{m\in\mathcal{M}} \sum_{e\in EP_d} P^{flow}_{wind,m,e,t} + \sum_{m\in\mathcal{M}} PB^{flow}_{wind,m,t} \le cf^{wind}_t \cdot D^R_{wind},\ \forall t \in \mathcal{T}, \tag{2s}$$

$$\sum_{r\in\mathcal{R}} PB^{flow}_{r,m,t} \cdot \eta^B = EB^{dem}_{m,t},\ \forall m \in \mathcal{M}, \forall t \in \mathcal{T}, \tag{2t}$$

$$EB^{dem}_{m,t} = R^{\mathrm{H_2O}}_{m,t} \cdot \Delta H^{\mathrm{H_2O}},\ \forall m \in \mathcal{M}, \forall t \in \mathcal{T}, \tag{2u}$$

$$D_{m,e} \ge E^{dem}_{m,e,t},\ \forall m \in \mathcal{M}, \forall e \in E_d \setminus \{reac\}, \forall t \in \mathcal{T}, \tag{2v}$$

$$D^B_m \ge EB^{dem}_{m,t},\ \forall m \in \mathcal{M}, \forall t \in \mathcal{T}, \tag{2w}$$

$$S^{\mathrm{H_2}}_1 = S^{\mathrm{H_2},i}, \tag{2x}$$

$$S^{\mathrm{H_2}}_{t+1} = S^{\mathrm{H_2}}_t + \sum_{m\in\mathcal{M}} PD^{\mathrm{H_2},tp}_{m,t} - Sup^{\mathrm{H_2}}_t,\ \forall t \in \mathcal{T} \setminus \{NT\}, \tag{2y}$$

$$Sup^{\mathrm{H_2}}_t = Dem^{\mathrm{H_2}}_t + Ex^{\mathrm{H_2}}_t,\ \forall t \in \mathcal{T} \setminus \{NT\}, \tag{2z}$$

$$D^{\mathrm{H_2}} \ge S^{\mathrm{H_2}}_t,\ \forall t \in \mathcal{T}, \tag{2aa}$$

$$-\epsilon^{tol} \cdot PD^{min} \le S^{\mathrm{H_2}}_1 - S^{\mathrm{H_2}}_{NT} \le \epsilon^{tol} \cdot PD^{min}, \tag{2ab}$$

$$Pur^{\mathrm{H_2}}_m = y^{a1}_{m,1},\ \forall m \in \mathcal{M}, \tag{2ac}$$

$$PD^{\mathrm{H_2}}_m = y^{a1}_{m,2}, \qquad \forall m \in \mathcal{M}, \tag{2ad}$$

$$R^{\mathrm{CH_4}}_{m,t} = z_{m,t,SR} \cdot y^{a1}_{m,3}, \qquad \forall m \in \mathcal{M}, \forall t \in \mathcal{T}, \tag{2ae}$$

$$R^{\mathrm{H_2O}}_{m,t} = z_{m,t,SR} \cdot y^{a1}_{m,4} + z_{m,t,purge} \cdot y^{a1}_{m,5} + z_{m,t,P} \cdot y^{a1}_{m,6},\ \forall m \in \mathcal{M}, \forall t \in \mathcal{T}, \tag{2af}$$

$$E^{dem}_{m,e,t} = \sum_{s\in\mathcal{S}} \sum_{n_1^{out}\in\mathcal{N}_1^{out}} z_{m,t,s} \cdot y^{a1}_{m,n_1^{out}} \cdot map^{p}_{e,s,n_1^{out}},$$

$$\forall m \in \mathcal{M}, \forall e \in E_d, \forall t \in \mathcal{T}, \tag{2ag}$$

$$E^{\mathrm{CO_2}}_{m,t} = z_{m,t,purge} \cdot y^{a1}_{m,30}, \qquad \forall m \in \mathcal{M}, \forall t \in \mathcal{T}, \tag{2ah}$$

$$D_{m,d} = x^{a2}_{m,n_2^{in}}, \qquad \forall m \in \mathcal{M}, \forall (d, n_2^{in}) \in map^{c1}_{d,n_2^{in}}, \tag{2ai}$$

$$x^{a1}_{m,n_1^{in}} = x^{a2}_{m,n_2^{in}}, \qquad \forall m \in \mathcal{M}, \forall (n_1^{in}, n_2^{in}) \in map^{pc}_{n_1^{in},n_2^{in}}. \tag{2aj}$$

Here, Eq. 2a denotes the objective function that consists of minimizing hydrogen production cost $C^{\mathrm{H_2}}$. Eq. 2a utilizes a normalized daily capital recovery factor $\phi^{cap,d}$ for computing the equivalent capital cost incurred in a day. It should be noted that the denominator consists of minimum production capacity PD^{min}, instead of actual production capacity $PD^{\mathrm{H_2},total}$, to maintain the MILP nature of the problem. Eqs. 2b and 2c represent the hydrogen product specifications in terms of minimum hydrogen product purity and production capacity, respectively. As the objective function expression Eq. 2a has PD^{min} in the denominator, the optimization model is incentivized to ensure $PD^{\mathrm{H_2},total}$ approximately equals PD^{min} to reduce overall costs. The overall amount of hydrogen produced during the scheduling horizon is calculated using Eq. 2d, whereas Eq. 2e computes the amount of hydrogen produced by module m at time t.

Eq. 2f computes the total installed cost TIC^T, which includes the costs of SE-SMR process equipment, co-located renewable farm, electric boiler and hydrogen storage tank. The total operating cost OC^T is calculated using Eq. 2g while considering the daily incurred costs of methane raw material, cooling utility, electricity and the revenue generated by carbon capture and utilization tax credit. The total installed costs for each individual equipment are calculated using Eqs. 2h-2l. Specifically, Eq. 2h computes the cost of SE-SMR process equipment by utilizing cost ANN model output $y^{a2}_{m,n_2^{out}}$. The electric feed heater cost is calculated using Eq. 2i. The costs of co-located renewable farm and electric boiler are obtained using Eqs. 2j and 2k, respectively. Eq. 2l computes the total installed cost of hydrogen storage tank. The individual cost components

for calculating daily operating costs and revenues are shown in Eqs. 2m-2p. Eqs. 2m and 2n denote the price of raw material methane and cooling water utility, respectively. The electricity price incurred during scheduling horizon is computed using Eq. 2o. Eq. 2p represents the revenue generated in terms of carbon capture and utilization tax credit minus the carbon transportation and storage costs.

The constraints Eq. 2q-2t denote the electricity power flow from energy sources to sinks. Particularly, Eq. 2q ensures that the energy demand for each equipment e in module m is met by energy sources throughout the scheduling horizon. Eqs. 2r and 2s constrain the maximum amount of power that can be withdrawn from solar and wind sources, respectively, by utlizing time-varying capacity factor values. The energy demand for electric boiler is met using Eq. 2t, and Eq. 2u computes the amount of energy required by electric boiler for stream generation. The design variables for equipment powered by electricity are obtained using Eqs. 2v-2w wherein their design capacity equals maximum power demand.

The design and operation of hydrogen storage tank is modeled using Eqs. 2x-2ab. Eq. 2x denotes the initial level of hydrogen in the storage tank. The hydrogen mass balance equation for the storage tank is represented by Eq. 2y. The amount of hydrogen produced by both modules is sent to the storage tank, and the incoming hydrogen is either accumulated in the tank or utilized for meeting consumer demand. An additional positive term, $Ex_t^{\mathrm{H_2}}$, is defined as a slack variable for balancing the hydrogen supply and demand mismatch (Eq. 2z). In physical terms, $Ex_t^{\mathrm{H_2}}$ denotes the excess hydrogen supply that is discarded due to lack of enough demand. Eq. 2aa computes the design capacity of storage tank, which is the maximum level of hydrogen stored. As the scheduling horizon consists of one representative day, the cyclic constraint Eq. 2ab is enforced such that the initial and final hydrogen levels are within a small tolerance. This ensures the validity of the overall process schedule for consecutive days of operation.

The input and output variables of process and cost ANN models are embed-

ded in the optimization problem through Eqs. 2ac-2aj. The hydrogen product purity and production rate are assigned using Eqs. 2ac and 2ad, respectively. The respective amounts of methane and steam consumed are calculated via Eqs. 2ae and 2af. The time-varying energy demand for SE-SMR process equipment is obtained using Eq. 2ag. In addition, Eq. 2ah computes the amount of carbon dioxide emitted during process purge steps. The equipment design variables and input variables to the cost ANN model are connected through Eq. 2ai. Finally, Eq. 2aj connects the input variables that are shared among the process and cost ANN models.

4. Case Studies

In this section, we demonstrate the proposed renewable-integrated hydrogen production process and the MILP-based optimization framework using regional and nationwide case studies for satisfying local hydrogen refueling demands. The analysis is firstly presented for Oakland, CA and later extended to a nationwide case study to investigate the impact of renewable availability, hydrogen demand and electricity price on hydrogen production costs.

4.1. Single Location Analysis: Oakland, CA

To demonstrate the design and scheduling framework, we utilize the renewable availability data for the Oakland city in California. We select this particular location as it has high availability of both solar and wind energy, with an average solar irradiance of 193.1 W/m^2 and an average wind speed of 4 m/s. In addition, the Oakland city also has localized hydrogen demand for transportation which is currently met through a retail hydrogen refueling station. The existing Oakland hydrogen refueling station is one of the ten stations that serve the San Francisco Bay Area.

To minimize the hydrogen production cost, we solve the MILP-based optimization model reported in Eqs. 2a-2aj, along with process and cost ANN model expressions reported in the Supplementary Data. The MILP problem

is programmed in GAMS 31.1 environment, and is solved using CPLEX 12.10 solver. All the computations are performed on a 2.5 GHz Intel Xeon CPU E5-2670 v2 processor. The overall model consists of 455,077 continuous decision variables, 200 binary decision variables, and 429,100 constraints. With a maximum running time of 1800 s, the CPLEX solver can obtain the globally optimal solution with an optimality gap of less than 0.1%.

The formulated optimization model assumes a 4-step SE-SMR cycle with fixed durations for each of the processing steps. To optimize the SE-SMR cycle step durations for SR and rPurge steps, we perform several optimization runs wherein the duration of these steps are varied in the range of 60 to 260 s in increments of 20 s. However, the duration of rDP and P steps are fixed to 20 s. Overall, this results in a set of 13 optimization runs as the step durations for SR and rPurge are assumed to be the same. In addition, the scaled inputs to the trained ANN models are varied between -0.9 and 0.9 such that the ends of the input space are removed. The revised bounds help in retaining the cross-validation accuracy as the models tend to predict poorly near input space boundaries.

To model the variation of demand during a representative day of the hydrogen fueling station, we refer to the recent study of Mansoor et al. [62] wherein they report a typical hourly hydrogen demand profile for a weekday to satisfy the fuel demands of an entire hydrogen fuel cell-powered fleet. Their analysis indicates that there is a high hydrogen demand during the day with 3 demand peaks in between 7 am and 1 pm. Conversely, there is a low hydrogen demand during the late evening and night hours. Using their study, we qualitatively utilize the temporal variation profile in the hydrogen demand and normalize it appropriately for producing 2 ton/day of hydrogen. Such a production capacity value is in accordance with the reported results for a realistic hydrogen refueling station operation [63]. Additionally, we obtain the daily variation profile of solar and wind energy availability by respectively computing the hourly average of solar irradiance and wind speed for each of the 24 hours using the yearly data from the NREL's National Solar Radiation Database (NSRDB). The database

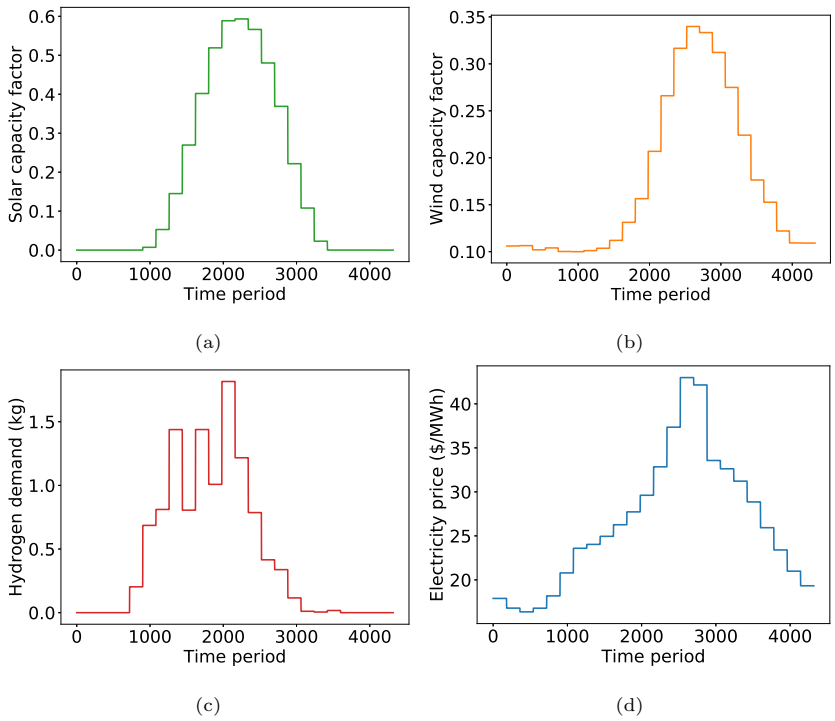

Figure 5: Daily input time series data for Oakland, CA denoting (a) solar PV capacity factor, (b) wind turbine capacity factor, (c) normalized hydrogen demand and (d) electricity price for each time period in the scheduling horizon.

includes the typical hourly-discretized weather conditions for 1020 weather stations, which has been computed using the historical observations for the last 30 years. Here, we specifically utilize the available weather data for Oakland, CA. To obtain the variation of electricity price during the day, we obtain the hourly average electricity price for each of the 24 hours using the yearly electricity data [50]. The resulting time series input data for solar and wind availability, hydrogen demand and electricity price for Oakland are shown in Figure 5.

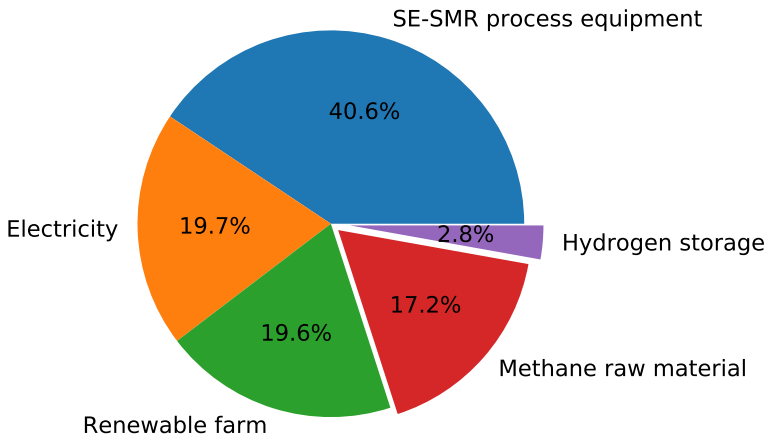

Figure 6: Hydrogen production cost breakdown for Oakland, CA with a production capacity of 0.5 ton/day and renewable price of $300/kW.

Using these input data profiles for a representative day, we solve the optimization problem for a futuristic scenario wherein renewables price has reduced to $300/kW. Such an analysis is useful in identifying the utilization of renewables under the best case scenario with the lowest renewables cost. The minimum hydrogen production cost obtained is $2.73/kg, and the breakdown of this cost is shown in Figure 6. It can be observed that the major cost components include the capital costs of SE-SMR process equipment and renewable farm with an overall cost contribution of 60.2%. The price of raw material methane also contributes significantly to the overall cost, with its share being 17.2%. The installation of renewable farm reduces the operating cost of purchasing electricity from the grid, which contributes 19.7% to the overall cost. As the design capacity of the hydrogen storage tank is optimized, it only has 2.8% share in the total cost.

The optimal results show that installing a co-located renewable farm, consisting of both wind and solar, is economical with a respective design capacity of 3622 and 8979 kW. The power flow schedule from renewables and grid to satisfy SE-SMR process energy demands is shown in Figure 7 for some specific hours in the day. On the y axis, the figure shows the total power requirement

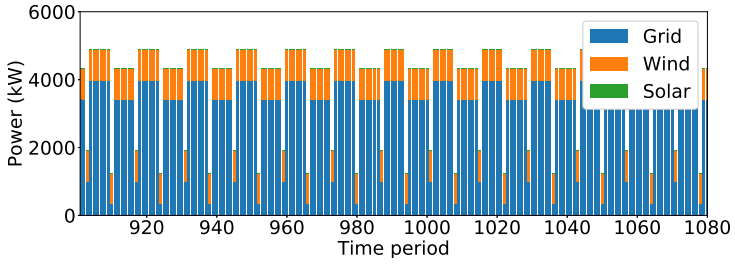

(a)

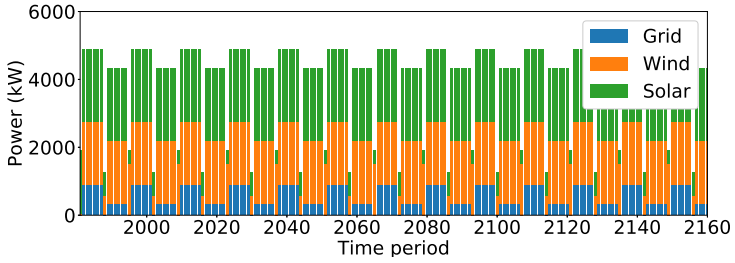

(b)

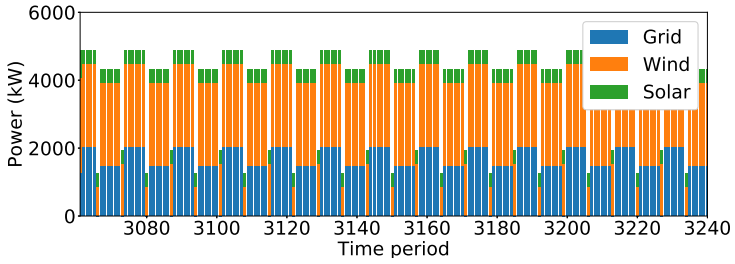

(c)

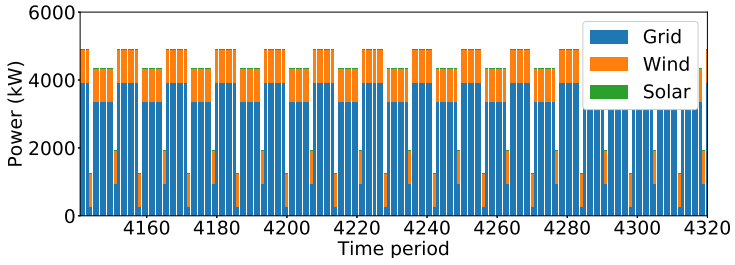

(d)

Figure 7: Optimal power flow schedule from electricity grid and renewables to meet SE-SMR process energy requirements for the representative day in Oakland, CA. The figure depicts the contribution of different energy sources during 4 representative hours in the day: (a) 6:00 - 7:00 am, (b) 12:00 - 1:00 pm, (c) 6:00 - 7:00 pm and (d) 12:00 - 1:00 am.

during each time period, and the contribution of energy sources to meet power demands. The total power requirement varies along the scheduling horizon due to multi-step operation of the SE-SMR process, and difference in the sizes of the two SE-SMR modules that are synchronously operated. As a fixed SE-SMR cycle is operated periodically, process power demands also showcase a periodically repeating pattern. During morning, late-evening and night hours, a majority of power demand is satisfied by electricity (sourced from grid) and wind sources as there is little solar energy available. However, during afternoon hours, the SE-SMR process runs almost entirely on renewable energy sources with grid satisfying only a small fraction of power demand. Overall, the grid, wind and solar sources meet 50.7%, 35% and 14.3% of the daily power demands of the SE-SMR process, respectively.

The optimal equipment design and operating variables for the 2 SE-SMR modules are reported in Table 1. Additionally, the analysis shows that the optimal SE-SMR cycle time is 280 seconds with SR and rPurge steps being 120 seconds long. The hydrogen production capacity for the two modules are approximately 4.2 and 2.3 kg H_2/cycle, which collectively result in a combined production capacity of 2 ton/day. The two modules are operated at a moderately high step 1 pressure of 177.8 and 154 kPa to balance the reaction and adsorption phenomena. This is because high pressure favors the adsorption of carbon dioxide on HTC adsorbent whereas reforming reactions are favored at low pressure. For both the modules, the optimizer selects the lowest possible purge velocity of 0.06 m/s, which leads to a lower energy consumption by the electric boiler for steam generation. A high adsorbent to catalyst ratio of 4.52 and 4.8 is selected in both the modules for increasing the *in-situ* capture of carbon dioxide to drive the reforming reactions towards hydrogen production. It can also be observed that for many of the compressors and coolers, the lowest possible design duty of 50 kW is obtained. Even though it leads to equipment overdesign, we do not reduce the lower bound on compressor and cooler duties to retain the accuracy of ANN models.

Table 1: Optimal equipment design and operating variables for the two SE-SMR modules.

Decision variable	Unit	Module 1	Module 2
Electric boiler design duty	kW	1559.6	932.2
Step 1 feed pressure	Pa	177848.9	154013.7
Step 1 feed superficial velocity	m/s	0.034	0.026
Step 3 feed superficial velocity	m/s	0.06	0.06
Adsorbent to catalyst ratio	-	4.52	4.8
Bed length	m	1.16	0.81
Number of tubes	-	3522	2161
Feed compressor design capacity	kW	106.1	50
Feed heater design capacity	kW	503.2	290.4
Outlet cooler design duty	kW	1936.5	1250
CO_2 compressor 1 design capacity	kW	50	50
CO_2 cooler 1 design duty	kW	739.1	389.2
CO_2 compressor 2 design capacity	kW	50	50
CO_2 cooler 2 design duty	kW	50	50
CO_2 compressor 3 design capacity	kW	50	50
CO_2 cooler 3 design duty	kW	50	50
H_2 compressor 1 design capacity	kW	129	62.8
H_2 cooler 1 design duty	kW	306.7	300.8
H_2 compressor 2 design capacity	kW	110.8	50
H_2 cooler 2 design duty	kW	107.3	50
H_2 compressor 3 design capacity	kW	110.8	50
H_2 cooler 3 design duty	kW	320.4	328.7

To meet the time-varying hydrogen demand, Figure 8 shows the hydrogen supply schedule along with the level of hydrogen in the storage tank. The hydrogen supply is equal to the sum of hydrogen demand met and the amount of hydrogen discarded. The discarded hydrogen variable is introduced to act as a slack variable, which makes it relatively easier to satisfy the cyclic constraint

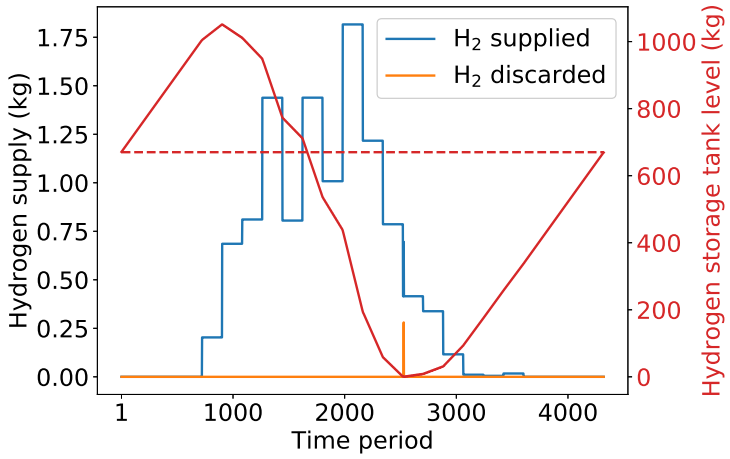

Figure 8: Optimal schedule of hydrogen supply and hydrogen storage tank level during the representative day in Oakland, CA.

on hydrogen tank level. In the beginning of the day, the hydrogen tank level is at 671.1 kg, and the cyclic constraint ensures that the tank level is the same at the end of the day. The SE-SMR modules are operated continuously during the entire scheduling horizon, thereby leading to a continuous production of hydrogen. During the evening and late-night hours, there is little hydrogen demand and a majority of the hydrogen manufactured is stored in the tank. The spike in hydrogen demand during the day hours is met through a combination of stored hydrogen along with the hydrogen produced in real time. The maximum hydrogen tank level of 1051.3 kg is obtained during the morning hours, which is also the hydrogen storage tank size. This is approximately half the amount of daily hydrogen demand thereby resulting in lower hydrogen storage costs. A small amount of hydrogen of 0.6 kg is discarded during the overall schedule. This possibly results in meeting the cyclic constraint condition, and/or reducing the size of the hydrogen storage tank.

The amount of carbon dioxide produced and captured depends on several factors including the amount of hydrogen produced by the SE-SMR reactor module, process operating conditions and reactor design. For this case study,

there is approximately 11.4 ton/day of carbon dioxide captured. This translates to 5.7 ton of carbon dioxide captured for every ton of hydrogen manufactured. There could be a variety of uses of the captured carbon dioxide as a raw material feedstock for manufacturing value-added fuels and chemicals, as an enhanced oil recovery agent and in the food and beverage industry [64, 65, 66, 67].

To ensure the validity of the optimization results obtained, we perform cross-validation by comparing the ANN model predictions with those of the high-fidelity model. In our experience, it is especially important to perform the validation at the optimal solution obtained as it often tends to have large cross-validation error. Figure S1 in the Supplementary Data shows the cross-validation plots for both SE-SMR process and cost ANN models. In case of SE-SMR model validation, a wide range of output values are obtained with different units. Therefore, the output magnitude has been reported in Figure S1a. For validating cost predictions, Figure S1b compares the output cost levels. There is an excellent agreement between the predictions of ANN and high-fidelity models, thereby validating the ANN models employed in the broader optimization problem.

4.2. Nationwide Analysis

There is a large variation is spatiotemporal availability of renewables across the United States. This can lead to significant variations in hydrogen production costs while utilizing renewable-integrated sustainable technologies. Figure 9 shows the variation in average solar irradiance and wind speed across the nation. The average weather data are obtained using the hourly-discretized weather conditions for 1020 weather stations from the NREL's NSRDB database. We can observe a large spatial variation in the availability of solar and wind resources. Particularly, there is abundant solar energy available in the southwestern states of California, Arizona, New Mexico, and Nevada. However, the northeastern region suffers from low solar energy availability. Similarly, wind energy also has a large variation with midwestern states of North Dakota, South Dakota, Nebraska, Kansas, and Oklahoma having the highest wind availability.

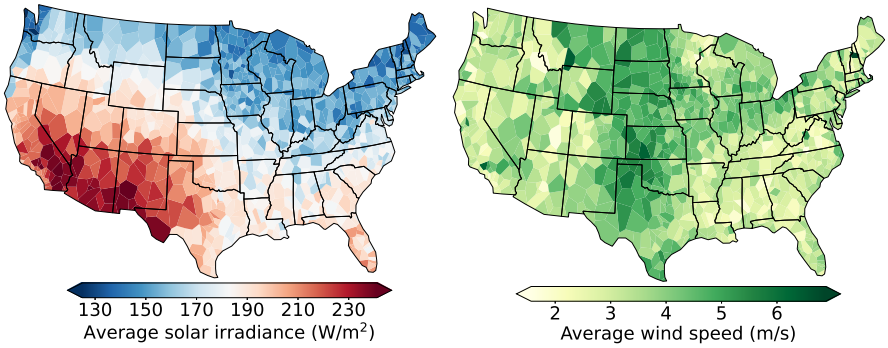

(a) (b)

Figure 9: Spatial variation of average (a) solar irradiance and (b) wind speed across the United States. For obtaining these figures, we specifically refer to the solar and wind availability in the NREL's National Solar Radiation Database (NSRDB) for 1020 weather stations. We compute the average of hourly solar irradiance and wind speed to depict the spatial variation in availability of these resources.

In addition to the spatial variations shown in weather data in Figure 9, there exists large temporal variations in their availability as well. For instance, there is no solar availability during night whereas wind speed is also significantly affected by time of day. The solar and wind availability also show variable seasonal patterns. Consequently, it necessitates the need for an optimization-based analysis that considers the spatiotemporal availability of wind and solar energy and determines the optimal renewable farm size for sustainable hydrogen manufacturing.

4.2.1. Effect of process scale

To this end, we perform an extensive nationwide analysis to determine the minimum hydrogen production cost at several different locations while meeting the hydrogen purity and production capacity constraints. Specifically, the optimization runs are performed for the 1020 sites in the United States for two different production capacity levels of 0.5 and 2 ton/day. For each location, the daily average for solar and wind availability is calculated using the yearly weather data which are obtained from the NREL's database. The daily hydro-

gen demand profile follows the same pattern as reported in Mansoor et al [62] with high demand during the day hours, and low demand during the evening and night hours. Even though the hydrogen demand pattern utilized is the same, the demand data are accordingly normalized to result in the overall daily production capacities of 0.5 and 2 ton/day. In addition, 13 individual optimization runs are performed with varying SR and rPurge step durations between 60 and 260 seconds such that the optimal step and cycle durations can be obtained. The future estimated renewable price of \$300/kW is utilized to obtain the lowest possible hydrogen production cost. Later, we also perform a sensitivity study to determine the effects of varying renewables price on hydrogen production cost.

The minimum hydrogen production cost obtained for the two different daily production capacity scenarios are shown in Figure 10. Additionally, Figure 10a-b show the optimal solar and wind farm design capacity with minimum daily production capacity of 0.5 ton/day, whereas Figure 10c-d denote the results for the 2 ton/day production capacity scenario. Due to the limitations of the software used (geopandas in python environment), the states of Alaska and Hawaii are excluded from the visualizations. It is also acceptable due to their remoteness and low demand which prevents large-scale utilization of renewable resources despite their abundant availability.

Due to the economies of scaling, the production scale of the process has a significant impact on the hydrogen production cost. Increasing the production scale from 0.5 ton/day to 2 ton/day leads to a decrease in the range of hydrogen production cost from \$3.6-\$4.2/kg H_2 to \$2-\$2.9/kg H_2, respectively, with the average production cost decreasing from \$4.1 kg/H_2 to \$2.7 kg/H_2. Additionally, for each of the two scenarios, we observe a variation in the hydrogen production cost across the United States due to variability in the availability of wind and solar energy. For instance, in the case of 2 ton/day production capacity, the average hydrogen production cost in the state of Kansas is \$2.5/kg H_2, whereas it increases to \$2.9/kg H_2 for the state of Maine.

There also exists a significant variation in the co-located renewable farm size depending on the geographical location and production scale of the process. For

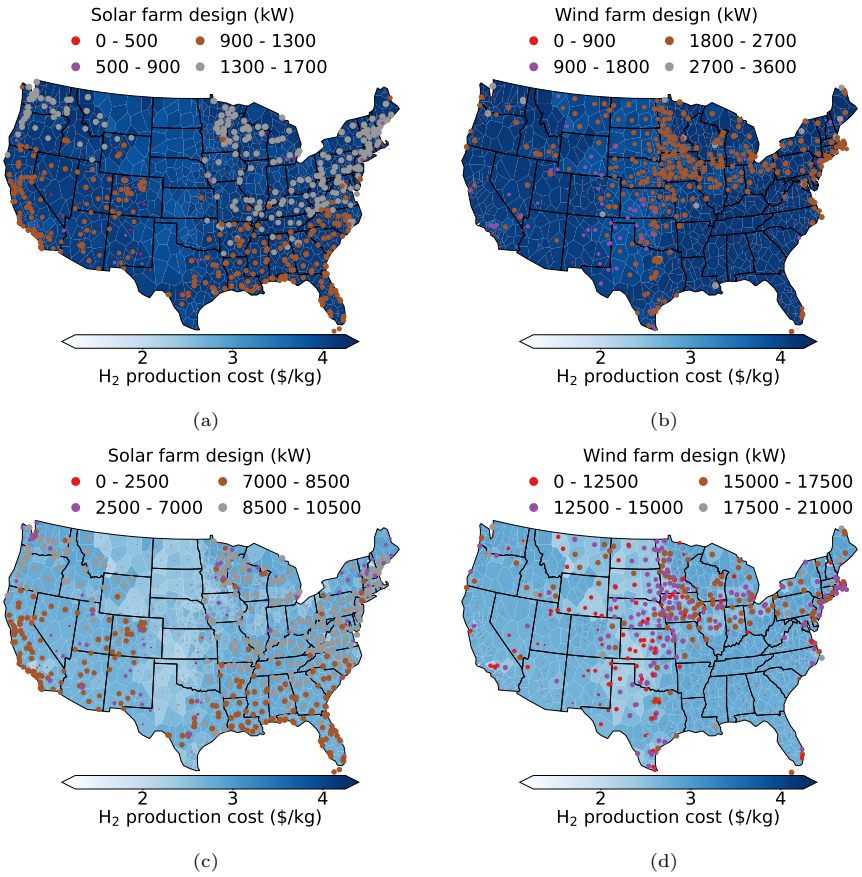

Figure 10: Minimum hydrogen production cost obtained for daily production capacity of (a-b) 0.5 ton/day and (c-d) 2 ton/day. The subfigures a and c show the optimal solar PV design capacity, and the subfigures b and d depict the optimal wind turbine size.

the 0.5 ton/day case, out of 1020 locations, solar PV is selected for 582 locations where the installed capacity varies in the range of 7.3-1666 kW and the average solar farm size is 1231.4 kW. On the other hand, wind turbines are selected for 447 locations. Typically, wind turbines size is bigger compared to solar PV with an average size of 2129 kW and range of 104.6-3463.9 kW. Both solar PV and wind turbine are selected for 45 locations. Compared to the results for the 0.5 ton/day case, the installed capacities of solar PV and wind turbine for 2 ton/day scenario are larger with an average capacity of 1931.4 kW and 3050.9

kW, respectively. The wind turbines are typically selected in midwestern and northeastern regions whereas solar PV dominates in the eastern, southeastern, and western regions (Figure 10).

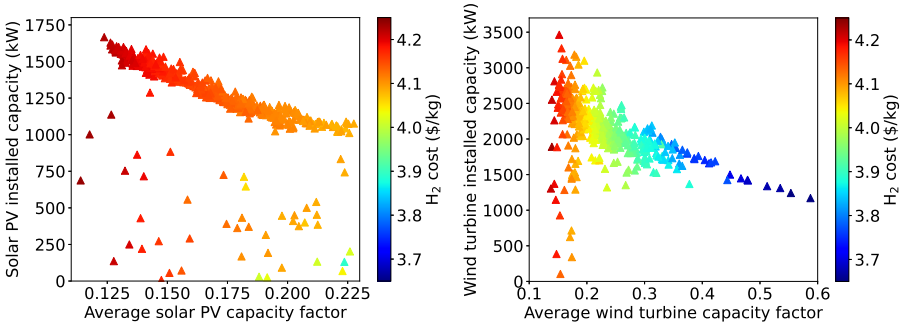

(a) (b)

Figure 11: Correlation of (a) solar PV and (b) wind turbine installed capacities with their respective average capacity factors for the 0.5 ton/day production capacity scenario.

For the 1020 locations, the correlation between the optimal installed capacities of renewables with their average capacity factors is shown in Figure 11 for the 0.5 ton/day production capacity scenario. It can be observed that there is an inverse relation between the two values such that increasing the average capacity factor reduces the installed capacity of solar PV and wind turbine. This is because the total power generated by a renewable source is obtained by multiplying capacity factor with installed capacity. Therefore, to obtain a specific amount of power, a lower installed capacity could be compensated by a higher capacity factor. The observations obtained here are in accordance with other studies reported in the literature that utilize renewables for hydrogen production [68]. For a few of the locations, we see some of the points in Figure 11 are significantly lower than the downward trending linear line. For instance, there are several locations where the solar PV installed capacity is lower than 900 kW whereas most of the locations have installed capacity in the range of 1000-1500 kW. This occurs due to the simultaneous selection of solar PV and wind turbine. Therefore, for the locations with lower than 900 kW solar PV

size, wind turbine is selected that also adds to the overall renewable generation capacity. A similar trend is observed for the locations with lower wind turbine capacities (<750 kW), wherein solar PV is also selected to compensate and add to the renewable-generated power.

To further investigate, we perform another set of optimization runs where only solar or wind can be selected. This avoids the simultaneous selection of solar and wind, and therefore helps us to better understand the absolute correlation between optimal installed capacities and average capacity factors if only one renewable technology is available. The correlations obtained are shown in Figure S2 in the Supplementary Data. For most of the locations, it is observed that the points approximately lie on the inversely-correlated linear line. This is because only one of the two renewable technologies can be selected for power generation which results in a higher installed capacity of individual renewable farms. This also explains the results obtained in Figure 11 where simultaneous selection of solar and wind technologies reduced their individual installed capacities for some locations. Conversely, in Figure S2, higher installed capacities of solar PV and wind turbine are obtained. On the other hand, there are a few locations with relatively lower renewable installed capacities. For instance, in case of solar PV, there are 4 locations with installed capacity less than 1150 kW and capacity factor less than 13%. In such cases, the selection of solar (or wind) does not significantly reduce the hydrogen production cost.

4.2.2. Effect of price of renewables

The previous analysis assumes the lowest price of renewables ($300/kW) that some studies estimate could be achieved in 2050s [50]. However, in the near future, the price of renewables will be higher. To investigate these scenarios, we perform a sensitivity analysis to obtain the effect of renewable price on hydrogen production cost and renewable farm size. The analysis is performed for three different solar PV and wind turbine prices of $300, $600 and $900/kW. For higher prices, it is observed that no renewables are selected and the SE-SMR process is powered entirely by electricity grid. Therefore, we select $900/kW

as the maximum renewable price. For each of the three cases, the optimization studies are performed for the 1020 locations while meeting a target production capacity of 1 ton/day.

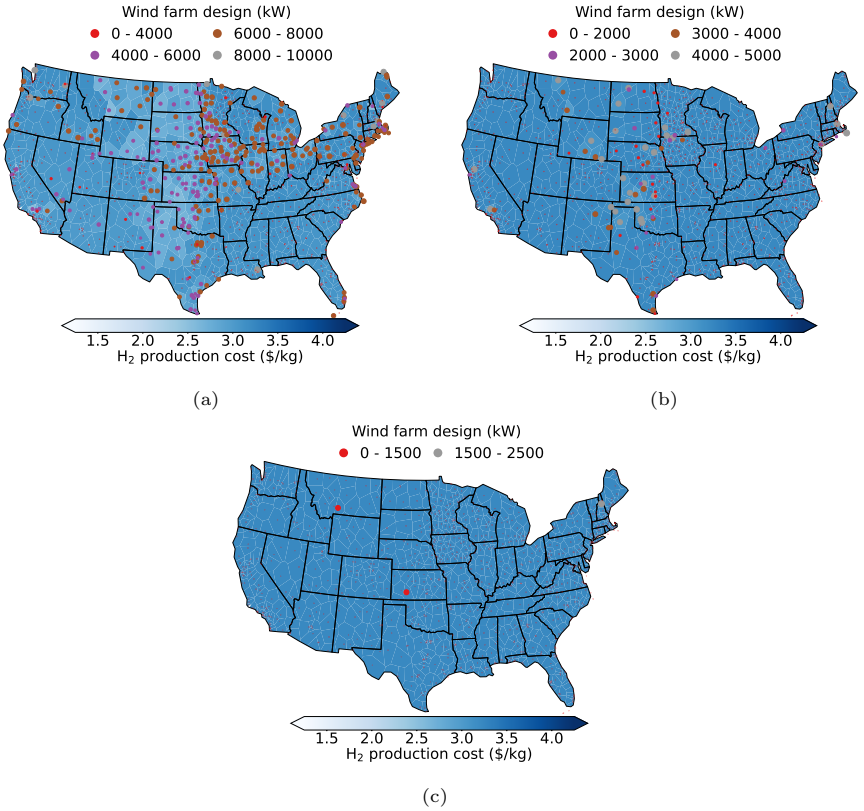

Figure 12: Hydrogen production cost and wind farm design capacities for varying renewable price of (a) \$300, (b) \$600 and (c) \$900 per kW. This figure specifically shows the wind farm design capacities as it is predominantly selected with larger design capacities compared to solar PV.

The resulting hydrogen production cost levels obtained are shown in Figure 12. Increasing renewable prices reduces the number of selected wind farms and the wind turbine design capacities and increases the hydrogen production cost. To illustrate, in the case of \$300/kW renewable price, wind turbines are selected for 445 locations with an average design capacity of 6024 kW. However, when the renewable price is increased to \$600/kW, the number of locations where

wind turbines are selected reduces to 109 with an average design capacity of 3335 kW. Further decreasing the renewable price to \$900/kW leads to only 3 locations with selected wind turbines. Figure 12 does not show the solar farm design capacities as solar is not selected for the \$600/kW and \$900/kW renewable price cases. However, for the \$300/kW case, solar PV size in the range of 25.3-4821.3 kW is selected for 610 locations. As smaller renewable farms are selected for higher renewable prices, the hydrogen production cost does not vary much. For the three renewable price levels of \$300, \$600 and \$900 per kW investigated here, the respective average hydrogen production cost is \$3.03, \$3.22 and \$3.23 per kg H_2. It should be particularly noted that the results obtained here are contingent upon the input electricity price profile. If the price of electricity provided by grid has higher cost, the installation capacity of solar PV and wind turbine will increase as it will be cheaper to produce power via co-located renewable farm.

4.2.3. Sensitivity analysis with varying prices of renewables, electricity and methane

Considering the existing and future variation in prices of solar PV and wind turbine, electricity, and methane, we perform a sensitivity analysis to investigate the effect of these varying input prices on hydrogen production cost. In the previous analysis, we imposed a time-varying electricity price profile. However, in the sensitivity analysis performed here, constant electricity price is assumed throughout the scheduling horizon. The case study on Oakland, CA is extended with a combination of the following input data values: (i) $c^{solar} = c^{wind} =$ \$300, \$450, \$600, ..., \$1500 per kW, (ii) $EP_t =$ \$10, \$50, \$100, ..., \$500 per MWh electricity for all $t \in \mathcal{T}$ and (iii) $P^{\mathrm{CH_4}} =$ \$0.1, \$0.3 and \$0.5 per kg methane. The bounds on these input data ranges are selected based on several literature studies [69, 70, 71, 72, 73, 74, 50]. To minimize the number of optimization runs, the cycle step durations are fixed to the previously-obtained optimal values of 120 s for SR and rPurge steps and 20 s for rDP and P steps. Overall, this results in a total of 297 optimization runs.

For a methane price of \$0.3/kg and a daily hydrogen production capacity of

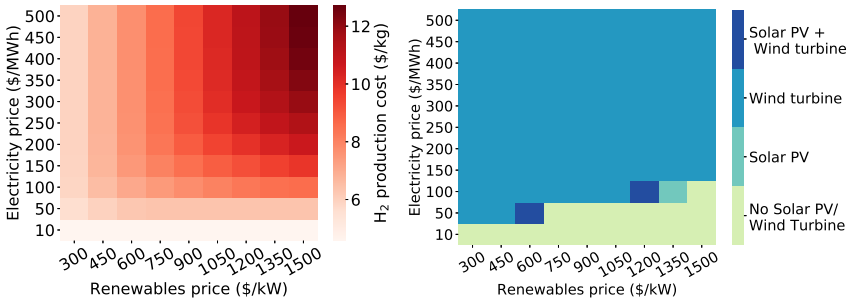

(a) (b)

Figure 13: Sensitivity analysis results depicting the effect of varying renewable and electricity prices on (a) hydrogen production cost and (b) renewable technology selected for power generation with $P^{\mathrm{CH_4}} = \$0.3$/kg and a production capacity of 0.5 ton/day for Oakland, CA.

500 kg/day, a production cost in the range \$4.1-12.2/kg H_2 is observed. The variation of hydrogen production cost with varying electricity and renewables prices is shown through a heatmap in Figure 13a. In addition, Figure 13b shows the renewable technology/technologies selected during the analysis. The optimizer does not select either solar or wind energy in the entire renewables price range for an electricity price of \$10/MWh. However, when electricity and renewables price vary between \$50-100/MWh and \$600-1350/kW, respectively, there exists an intersection of 3 different regions where only solar, only wind or both solar and wind technologies are selected. For an electricity price higher than \$100/MWh, only the wind turbine technology is selected regardless of the price of renewables. Furthermore, the sensitivity results presented in Figure 13 do not change qualitatively with varying methane feedstock price. However, increasing methane price results in higher hydrogen production cost. To illustrate, increasing the methane price from \$0.1 to \$0.5 per kg results in increasing the range of hydrogen production cost from \$3.6-11.7 to \$4.6-12.7 per kg H_2. It should be further noted that these results are only obtained for Oakland, CA. A similar analysis for another location with different solar and wind availability may lead to different results from what is shown here.

4.3. Effect of City-wise Hydrogen Demand on Cost

The previous analysis assumed a fixed daily hydrogen production capacity and demand across the United States. However, there will exist a significant variation in the amount of hydrogen required in different cities and at different refueling stations. The major factors that can impact the hydrogen demand include city population, daily average commute distances and number of vehicles owned per person. In addition, another factor that needs to be analyzed more extensively is the penetration of hydrogen vehicles. Depending on the maturity of HFCEV markets, the hydrogen demand can vary significantly. Therefore, it becomes imperative to consider the city-wise variation in hydrogen demand in the overall nationwide analysis under different HFCEV market penetration scenarios.

To perform this analysis, we refer to the hydrogen delivery scenario analysis model (HDSAM) developed and maintained by the Argonne National Laboratory [75]. Although the HDSAM tool is developed to estimate and compare the hydrogen refueling cost under different transportation and market scenarios, we leverage it for estimating the daily hydrogen demand at different locations across the United States. HDSAM takes several inputs for estimating hydrogen fuel demand including city population, average commute distance and number of vehicles owned per person. Therefore, HDSAM considers both the population and economic prosperity of a region to estimate hydrogen demand. For our study, we obtain the daily hydrogen demand data for 448 urban cities under 4 different HFCEV market penetration levels of 1%, 5%, 10% and 20% (Figure 14). To simplify the analysis, for a single city, it is assumed that a large renewable-integrated SE-SMR plant serves multiple refueling stations in the city and the maximum production capacity of the individual SE-SMR plant is 8 ton/day. If the city-wide hydrogen demand exceeds 8 ton/day, multiple SE-SMR plants are developed to satisfy the hydrogen demand for the refueling stations in the city. The number of SE-SMR plants is obtained by dividing the city-wide daily hydrogen demand by 8 ton/day and applying the ceiling function on the resulting number. The production capacity for each of those SE-SMR

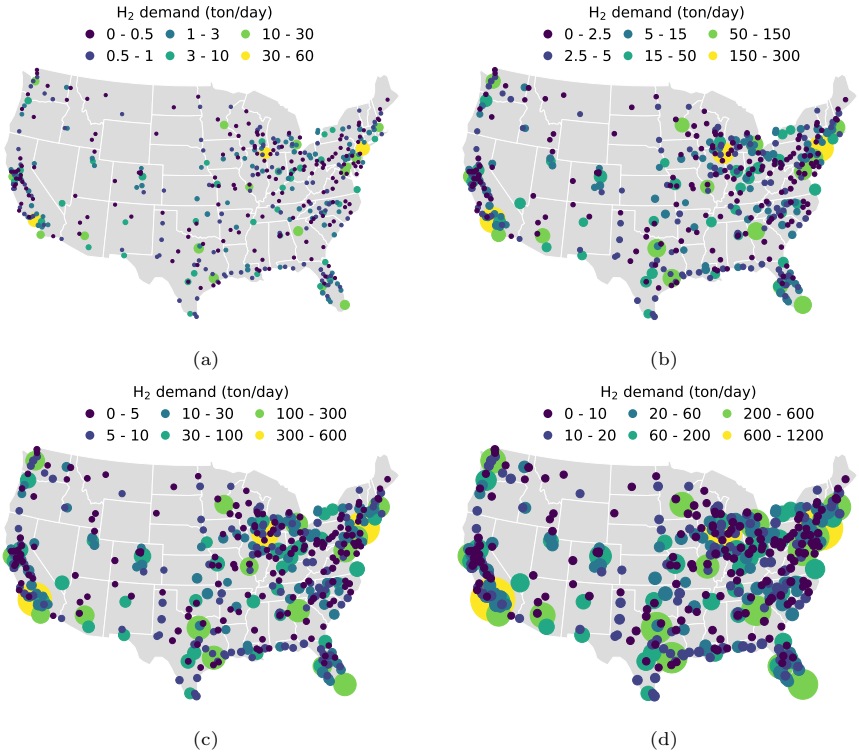

Figure 14: City-wise variation in daily hydrogen demand for different penetration levels of hydrogen vehicles: (a) 1%, (b) 5%, (c) 10% and (d) 20%. The data visualized here is obtained using the hydrogen delivery scenario analysis model (HDSAM) developed by the Argonne National Laboratory [75].

plants is then obtained by dividing the total hydrogen demand by the number of SE-SMR plants. In addition, minimum price of renewables is taken during the analysis, i.e., \$300/kW.

The minimum hydrogen production cost results are presented in Figure 15 for the 4 market penetration levels of HFCEV. The corresponding solar and wind farm design capacities are shown in Figures S3-S4 in the Supplementary Data. The hydrogen cost depends significantly on the market demand, and therefore, varying levels of HFCEV penetration result in drastically different hydrogen production costs. For example, the hydrogen production cost averaged over all 448 cities decreases from \$4/kg to \$2.5/kg when the HFCEV penetration level

Table 2: Top 20 cities with minimum hydrogen production cost for 1% hydrogen vehicle penetration scenario.

City	State	H_2 demand (ton/day)	H_2 cost ($/kg)	Wind design capacity (kW)	Solar design capacity (kW)
Bridgeport	CT	4.46	2.19	27866	0
Richmond	VA	4.2	2.19	26108.76	0
Buffalo	NY	3.98	2.24	22405.02	0
McAllen	TX	3.11	2.25	19509.68	0
Sarasota	FL	2.87	2.26	17903.53	0
Jacksonville	FL	4.76	2.27	30229.06	0
New Orleans	LA	3.64	2.27	23413.36	0
Grand Rapids	MI	2.85	2.28	15560.92	0
Springfield	MA	2.83	2.28	15474.46	0
San Antonio	TX	5.91	2.29	38403.3	0
New Haven	CT	2.66	2.29	16448.81	0
Albany	NY	2.74	2.29	15102.48	0
Tampa	FL	12.83	2.3	42000.82	0
Detroit	MI	19.13	2.3	36536.36	0
Minneapolis	MN	12.31	2.3	34971.23	0
Austin	TX	5.3	2.31	35152.53	0
Milwaukee	WI	6.4	2.31	36697.87	0
Seattle	WA	12.97	2.31	37326.53	0
Boston	MA	16.96	2.32	32271.51	0
Providence	RI	5.39	2.33	30626.54	0

increases from 1% to 20%. Similarly, with this increase in hydrogen penetration level, the maximum hydrogen production cost observed across all the cities

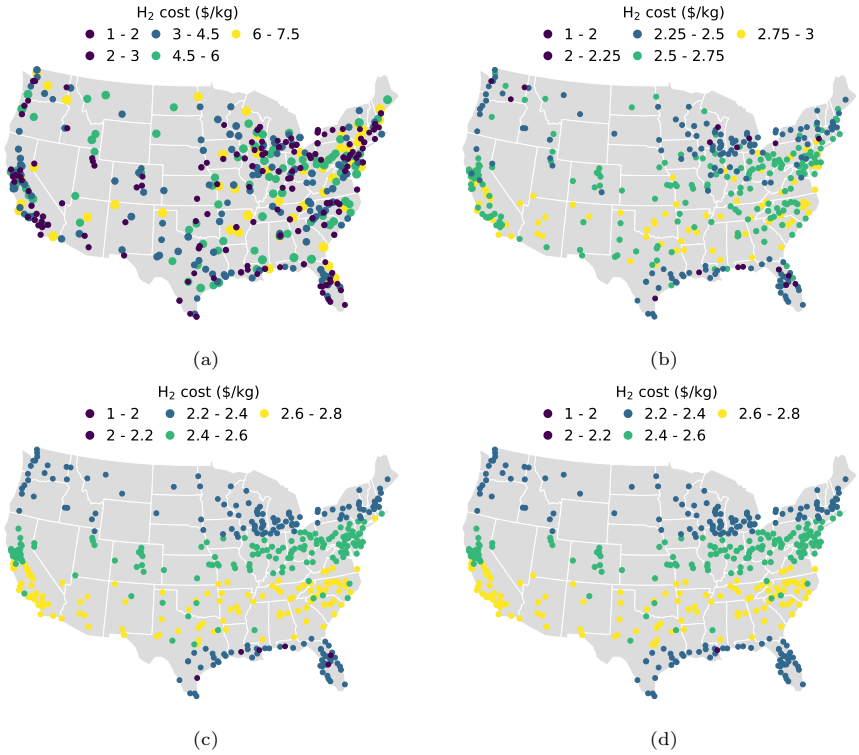

Figure 15: Regional variation of hydrogen production cost with different HFCEV penetration levels: (a) 1%, (b) 5%, (c) 10% and (d) 20% and renewable price of $300/kW.

reduces significantly from $7.1/kg to $2.8/kg. These results denote a large dependence of hydrogen production cost on hydrogen demand. This is further illustrated by the hydrogen production costs obtained for different cities. The large urban cities with high hydrogen demand, such as California, Texas, Florida and northeast region, have lower hydrogen costs. Conversely, for cities with less dense population in the states such as Arkansas, Tennessee and Arizona, lower hydrogen demand results in higher production costs.

Through the analysis, the top 20 cities obtained with minimum hydrogen production cost for the 1% HFCEV penetration case are reported in Table 2. The major reasons behind the low hydrogen production cost include high hydrogen demand, and high wind capacity factors. Wind turbine is selected as

the choice of renewable technology for all the cities. For the locations reported in Table 2, the installed capacity of wind turbine is in the range of 15-42 MW, and the highly ranked cities have lower wind installed capacities. This is possibly due to higher wind capacity factors, which do not lead to selection of larger wind design capacities. This observation is in accordance with the installed capacity-capacity factor correlations described earlier (Figure 11) wherein higher average capacity factors resulted in lower renewable installed capacities.

Beyond a hydrogen market penetration level, the production cost does not depend as much on the hydrogen demand amount which can be observed in Figure 15. For instance, there is little change in city-wise hydrogen production cost results when the hydrogen vehicle penetration level increases from 10% to 20%. This is due to the maximum production capacity threshold of an individual SE-SMR plant. For increasing hydrogen demand levels, the production capacity of each SE-SMR plant gets closer to its maximum capacity limit. Therefore, the cost reduction benefits offered by the economies of scaling reduces with increasing process scale. Consequently, we do not observe significant variation in hydrogen production cost results among higher HFCEV penetration level scenarios.

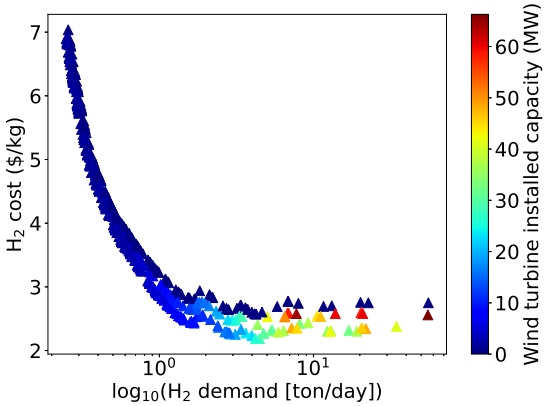

Figure 16: Correlation between hydrogen production cost and daily hydrogen demand for the city-wise analysis with 1% HFCEV penetration level.

Additionally, we observe that hydrogen production cost has a much stronger

dependence on hydrogen demand, and not the availability of solar or wind resources. To demonstrate this, we plot the hydrogen production cost vs hydrogen demand for the 448 cities and 1% HFCEV penetration scenario in Figure 16. Here, it can be clearly observed that with an increase in hydrogen demand, the hydrogen production cost falls rapidly. However, the advantages of increased hydrogen production scale decreases beyond the production capacity level of 2 ton/day. As wind is the dominant renewable technology selected, the figure also shows the installed capacities of wind turbine. It can be seen that the selection of wind technology reduces the hydrogen production cost, but the reduction is not as significant as is observed during process scale-up. Consequently, the hydrogen cost curve follows an exponentially decreasing trend with an increase in hydrogen demand without any significant dispersion due to the selection of wind turbines. However, this trend is not observed for higher HFCEV market penetration levels as the economic opportunities achievable through process scale-up diminish with increasing hydrogen demand amounts.

5. Conclusions

The major reasons preventing the widescale deployment of Hydrogen Fuel Cell Electric Vehicles (HFCEVs) are the high hydrogen fuel cost and the lack of extensive hydrogen refueling infrastructure. The high hydrogen transportation costs and the existing centralized nature of hydrogen production result in high hydrogen fuel prices to consumers. For small-scale and cost-effective hydrogen production, we proposed an intensified, small-scale and renewable-powered hydrogen production technology that can be deployed on-site to fulfill local hydrogen demand of refueling stations. The intensified SE-SMR technology has higher reaction conversion and product purity, lower temperature requirements and more efficient heat integration compared to SMR. In addition, the incorporation of process intensification principles in the SE-SMR process enables full electrification of the process. The required process energy demands are met through a combination of solar, wind and electricity grid sources.

We performed extensive regional and nationwide case studies to investigate whether a small-scale SE-SMR process is capable of meeting local hydrogen fuel cost targets. For the analysis, we developed a detailed computational framework based on a large-scale mixed integer linear programming (MILP) model for simultaneous design and scheduling of SE-SMR process while handling the spatiotemporal variability in renewable availability, and electricity price and hydrogen demand markets. To efficiently handle the computational complexities involved, an artificial neural network (ANN) model was developed and incorporated in the overall MILP model to accurately describe the SE-SMR process dynamics and nonlinear capital cost expressions.

The hydrogen cost minimization analysis indicates that the SE-SMR process can indeed result in low hydrogen production costs even at small process scales. Specifically, with futuristic renewable prices and a daily production capacity of 2 ton/day, a hydrogen production cost in the range \$2-\$2.9/kg H_2 is achievable across the United States. Decreasing the production scale of the process to 0.5 ton/day results in an increase in the hydrogen production cost range to \$3.6-\$4.2/kg H_2. The variation in hydrogen production cost is observed across the United States due to spatiotemporal variation in wind and solar availability. Typically, compared to solar PV, wind turbine is selected with higher average design capacity and more cost savings. We also observe an inverse correlation between the optimal design capacities of solar and wind farm, and their respective average capacity factors.

For small-scale and localized hydrogen manufacturing, the production cost also depends strongly on the local hydrogen demand level. Therefore, we performed a city-wise analysis wherein we estimate the hydrogen demand for 448 urban cities in the United States using the hydrogen delivery scenario analysis model (HDSAM) under different HFCEV market penetration scenarios [75]. The results demonstrate that hydrogen production cost has a much stronger dependence on hydrogen demand compared to other less significant factors such as price of renewables. Consequently, increasing the HFCEV market penetration level from 1% to 20% decreases the average hydrogen production cost from

$4 to $2.5 per kg H_2. Additionally, we observe that just 5% HFCEV market penetration level is sufficient to bring down the hydrogen production cost to less than $3/kg H_2 across all the urban cities in the United States.

Despite the advantages of deploying renewable-powered SE-SMR process showcased here for small-scale and sustainable hydrogen manufacturing, there are several challenges that need to be resolved before deployment of this technology commercially. Specifically, the dynamic SE-SMR process is more difficult to operate compared to the conventional steady-state SMR process due to multi-step and multi-cycle operation. Moreover, there could be challenges in retaining the effectiveness of the catalyst/adsorbent material mixture for facilitating SE-SMR reactions and capturing carbon dioxide, respectively, over long duration of operation. From a process control perspective, it is more challenging to develop a closed-loop controller to guarantee hydrogen product specifications are met due to the complexities and dynamics of underlying hybrid adsorption-reaction process.

Therefore, additional research endeavors are required for design of sorbent-catalyst hybrid materials for SE-SMR, devising optimal adsorbent regeneration scheme, and integrated design, scheduling, and control of dynamic SE-SMR systems. Furthermore, sustainable SE-SMR processes that are fully powered by wind and solar and are disconnected from grid, can also be developed as such processes would be vital to satisfy hydrogen demands in remote locations or where grid connectivity is not possible. Such a process scheme warrants further research for developing sophisticated algorithms and solution strategies due to more complicated on-off dynamic operation of the methane reforming modules.

Acknowledgements

The authors gratefully acknowledge funding support from the U.S. Department of Energy (Grant number DE-FE0031771) and the U.S. National Science Foundation (CAREER Award CBET-1943479). Part of this research was conducted with the advanced computing resources provided by Texas A&M High

Performance Research Computing.

References

[1] L. Michaelis, O. Davidson, GHG mitigation in the transport sector, Energy Policy 24 (10-11) (1996) 969–984.

[2] M. Muratori, T. Mai, The shape of electrified transportation, Environmental Research Letters 16 (1) (2020) 011003.

[3] S. Sharma, S. K. Ghoshal, Hydrogen the future transportation fuel: From production to applications, Renewable and sustainable energy reviews 43 (2015) 1151–1158.

[4] A. Negi, M. Mathew, Study on sustainable transportation fuels based on green house gas emission potential, in: 2018 International Conference on Power Energy, Environment and Intelligent Control (PEEIC), IEEE, 2018, pp. 420–424.

[5] C. Acar, I. Dincer, The potential role of hydrogen as a sustainable transportation fuel to combat global warming, International Journal of Hydrogen Energy 45 (5) (2020) 3396–3406.

[6] A. Demirbas, Present and future transportation fuels, Energy Sources, Part A 30 (16) (2008) 1473–1483.

[7] S. Kumarappan, S. Joshi, Trading greenhouse gas emission benefits from biofuel use in us transportation: Challenges and opportunities, Biomass and Bioenergy 35 (11) (2011) 4511–4518.

[8] P. Cuda, I. Dincer, G. Naterer, Hydrogen utilization in various transportation modes with emissions comparisons for ontario, canada, International Journal of Hydrogen Energy 37 (1) (2012) 634–643.

[9] I. Jain, Hydrogen the fuel for 21st century, International Journal of Hydrogen Energy 34 (17) (2009) 7368–7378.

[10] H. Fayaz, R. Saidur, N. Razali, F. Anuar, A. Saleman, M. Islam, An overview of hydrogen as a vehicle fuel, Renewable and Sustainable Energy Reviews 16 (8) (2012) 5511–5528.

[11] Y. S. Najjar, Hydrogen safety: The road toward green technology, International Journal of Hydrogen Energy 38 (25) (2013) 10716–10728.

[12] W. Colella, M. Jacobson, D. Golden, Switching to a us hydrogen fuel cell vehicle fleet: The resultant change in emissions, energy use, and greenhouse gases, Journal of Power Sources 150 (2005) 150–181.

[13] A. Elgowainy, K. Reddi, D.-Y. Lee, N. Rustagi, E. Gupta, Techno-economic and thermodynamic analysis of pre-cooling systems at gaseous hydrogen refueling stations, international journal of hydrogen energy 42 (49) (2017) 29067–29079.

[14] Number of hydrogen fuel stations in the U.S. 2019-2030, https://www.statista.com/statistics/1179571/us-number-of-hydrogen-fuel-stations/, accessed on May 19, 2021.

[15] S. A. Shaheen, E. Martin, T. E. Lipman, Dynamics in behavioral response to fuel-cell vehicle fleet and hydrogen fueling infrastructure: an exploratory study, Transportation Research Record 2058 (1) (2008) 155–162.

[16] B. C. Langford, C. Cherry, Transitioning a bus transit fleet to hydrogen fuel: A case study of knoxville area transit, International Journal of Hydrogen Energy 37 (3) (2012) 2635–2643.

[17] K. Reddi, M. Mintz, A. Elgowainy, E. Sutherland, Building a hydrogen infrastructure in the united states, in: Compendium of Hydrogen Energy, Elsevier, 2016, pp. 293–319.

[18] D. Symes, J. G. Maillard, J. Courtney, J. Watton, A. Meadowcroft, A. S. Chandan, L. Gurley, R. Priestly, G. Serdaroglu, Development of a hydrogen fuelling infrastructure in the Northeast USA (2014).

[19] K. Reddi, A. Elgowainy, N. Rustagi, E. Gupta, Impact of hydrogen refueling configurations and market parameters on the refueling cost of hydrogen, International Journal of Hydrogen Energy 42 (34) (2017) 21855–21865.

[20] E. Efficiency, R. Energy, A national vision of america's transition to a hydrogen economy—to 2030 and beyond (2002).

[21] E. Miller, C. Ainscough, A. Talapatra, Doe hydrogen and fuel cells program record: Hydrogen production status 2006–2013 (2014).

[22] D. Jakobsen, V. Åtland, Concepts for large scale hydrogen production, Master's thesis, NTNU (2016).

[23] S. Satyapal, R. Farmer, Doe hydrogen and fuel cells program record (2015).

[24] A. Arora, Process design, optimization and material screening methods for small-scale chemical manufacturing with application to unconventional natural gas, Ph.D. thesis (2021).

[25] S. E. Demirel, J. Li, M. M. F. Hasan, Systematic process intensification using building blocks, Computers & Chemical Engineering 105 (2017) 2–38.

[26] Y. Tian, S. E. Demirel, M. M. F. Hasan, E. N. Pistikopoulos, An overview of process systems engineering approaches for process intensification: State of the art, Chemical Engineering and Processing-Process Intensification 133 (2018) 160–210.

[27] S. E. Demirel, J. Li, M. El-Halwagi, M. M. F. Hasan, Sustainable process intensification using building blocks, ACS Sustainable Chemistry & Engineering 8 (48) (2020) 17664–17679.

[28] B. Carvill, J. Hufton, M. Anand, S. Sircar, Sorption-enhanced reaction process, AIChE Journal 42 (10) (1996) 2765–2772.

[29] J. Hufton, S. Mayorga, S. Sircar, Sorption-enhanced reaction process for hydrogen production, AIChE Journal 45 (2) (1999) 248–256.

[30] A. Arora, S. S. Iyer, M. M. F. Hasan, Grams: A general framework describing adsorption, reaction and sorption-enhanced reaction processes, Chemical Engineering Science 192 (2018) 335–358.

[31] A. Arora, I. Bajaj, S. S. Iyer, M. M. F. Hasan, Optimal synthesis of periodic sorption enhanced reaction processes with application to hydrogen production, Computers & Chemical Engineering 115 (2018) 89–111.

[32] C. Han, D. P. Harrison, Simultaneous shift reaction and carbon dioxide separation for the direct production of hydrogen, Chemical Engineering Science 49 (24) (1994) 5875–5883.

[33] W. E. Waldron, J. Hufton, S. Sircar, Production of hydrogen by cyclic sorption enhanced reaction process, American Institute of Chemical Engineers. AIChE Journal 47 (6) (2001) 1477.

[34] G.-h. Xiu, P. Li, A. E. Rodrigues, Sorption-enhanced reaction process with reactive regeneration, Chemical engineering science 57 (18) (2002) 3893–3908.

[35] K. Johnsen, H. Ryu, J. Grace, C. Lim, Sorption-enhanced steam reforming of methane in a fluidized bed reactor with dolomite as CO_2-acceptor, Chemical Engineering Science 61 (4) (2006) 1195–1202.

[36] Z.-s. Li, N.-s. Cai, Modeling of multiple cycles for sorption-enhanced steam methane reforming and sorbent regeneration in fixed bed reactor, Energy & Fuels 21 (5) (2007) 2909–2918.

[37] L. Barelli, G. Bidini, F. Gallorini, S. Servili, Hydrogen production through sorption-enhanced steam methane reforming and membrane technology: a review, Energy 33 (4) (2008) 554–570.

[38] D. P. Harrison, Sorption-enhanced hydrogen production: a review, Industrial & Engineering Chemistry Research 47 (17) (2008) 6486–6501.

[39] B. Dou, C. Wang, Y. Song, H. Chen, B. Jiang, M. Yang, Y. Xu, Solid sorbents for in-situ CO_2 removal during sorption-enhanced steam reforming process: A review, Renewable and Sustainable Energy Reviews 53 (2016) 536–546.

[40] A. Di Giuliano, K. Gallucci, Sorption enhanced steam methane reforming based on nickel and calcium looping: a review, Chemical Engineering and Processing-Process Intensification 130 (2018) 240–252.

[41] Y. Yan, D. Thanganadar, P. T. Clough, S. Mukherjee, K. Patchigolla, V. Manovic, E. J. Anthony, Process simulations of blue hydrogen production by upgraded sorption enhanced steam methane reforming (SE-SMR) processes, Energy Conversion and Management 222 (2020) 113144.

[42] S. T. Wismann, J. S. Engbæk, S. B. Vendelbo, F. B. Bendixen, W. L. Eriksen, K. Aasberg-Petersen, C. Frandsen, I. Chorkendorff, P. M. Mortensen, Electrified methane reforming: A compact approach to greener industrial hydrogen production, Science 364 (6442) (2019) 756–759.

[43] M. Rieks, R. Bellinghausen, N. Kockmann, L. Mleczko, Experimental study of methane dry reforming in an electrically heated reactor, International Journal of Hydrogen Energy 40 (46) (2015) 15940–15951.

[44] J. K. Dahl, A. W. Weimer, A. Lewandowski, C. Bingham, F. Bruetsch, A. Steinfeld, Dry reforming of methane using a solar-thermal aerosol flow reactor, Industrial & Engineering Chemistry Research 43 (18) (2004) 5489–5495.

[45] M. Abele, A. Wörner, G. Brose, R. Buck, R. Tamme, Test results of a receiver reactor for solar methane reforming and aspects of further applications of this technology (1997).

[46] A. Wörner, R. Tamme, CO_2 reforming of methane in a solar driven volumetric receiver–reactor, Catalysis today 46 (2-3) (1998) 165–174.

[47] M. Levy, R. Levitan, H. Rosin, R. Rubin, Solar energy storage via a closed-loop chemical heat pipe, Solar Energy 50 (2) (1993) 179–189.

[48] T. Kodama, T. Koyanagi, T. Shimizu, Y. Kitayama, CO_2 reforming of methane in a molten carbonate salt bath for use in solar thermochemical processes, Energy & fuels 15 (1) (2001) 60–65.

[49] S. G. Mayorga, J. R. Hufton, S. Sircar, T. Gaffney, Sorption enhanced reaction process for production of hydrogen. phase 1 final report, Tech. rep., Air Products and Chemicals, Inc., Allentown, PA (United States) (1997).

[50] M. S. Zantye, A. Arora, M. F. Hasan, Renewable-integrated flexible carbon capture: a synergistic path forward to clean energy future, Energy & Environmental Science (2021).

[51] M. Zachar, M. Trifkovic, P. Daoutidis, Policy effects on microgrid economics, technology selection, and environmental impact, Computers & Chemical Engineering 81 (2015) 364–375.

[52] C. L. Archer, M. Z. Jacobson, Spatial and temporal distributions of us winds and wind power at 80 m derived from measurements, Journal of Geophysical Research: Atmospheres 108 (D9) (2003).

[53] A. Allman, P. Daoutidis, Optimal scheduling for wind-powered ammonia generation: Effects of key design parameters, Chemical Engineering Research and Design 131 (2018) 5–15.

[54] A. Arora, S. S. Iyer, I. Bajaj, M. M. F. Hasan, Optimal methanol production via sorption-enhanced reaction process, Industrial & Engineering Chemistry Research 57 (42) (2018) 14143–14161.

[55] V. Dua, A mixed-integer programming approach for optimal configuration of artificial neural networks, Chemical Engineering Research and Design 88 (1) (2010) 55–60.

[56] M. Fischetti, J. Jo, Deep neural networks and mixed integer linear optimization, Constraints 23 (3) (2018) 296–309.

[57] B. Grimstad, H. Andersson, ReLU networks as surrogate models in mixed-integer linear programs, Computers & Chemical Engineering 131 (2019) 106580.

[58] P. Pimporn, S. Kittipiyakul, J. Kudtongngam, H. Fujita, Missing value estimation of energy consumption of multi-unit air conditioners using artificial neural networks, in: 2018 International Conference on Embedded Systems and Intelligent Technology & International Conference on Information and Communication Technology for Embedded Systems (ICESIT-ICICTES), IEEE, 2018, pp. 1–5.

[59] I. El Jaafari, A. Ellahyani, S. Charfi, Parametric rectified nonlinear unit (PRenu) for convolution neural networks, Signal, Image and Video Processing (2020) 1–6.

[60] D. P. Kingma, J. Ba, Adam: A method for stochastic optimization, arXiv preprint arXiv:1412.6980 (2014).

[61] A. Gulli, S. Pal, Deep learning with Keras, Packt Publishing Ltd, 2017.

[62] M. Mansoor, M. Stadler, H. Auer, M. Zellinger, Advanced optimal planning for microgrid technologies including hydrogen and mobility at a real microgrid testbed, International Journal of Hydrogen Energy (2021).

[63] N. Liu, F. Xie, Z. Lin, M. Jin, Evaluating national hydrogen refueling infrastructure requirement and economic competitiveness of fuel cell electric long-haul trucks, Mitigation and Adaptation Strategies for Global Change (2019) 1–17.

[64] B. Metz, O. Davidson, H. De Coninck, et al., Carbon dioxide capture and storage: special report of the intergovernmental panel on climate change, Cambridge University Press, 2005.

[65] E. Esposito, L. Dellamuzia, U. Moretti, A. Fuoco, L. Giorno, J. C. Jansen, Simultaneous production of biomethane and food grade CO_2 from biogas: An industrial case study, Energy & Environmental Science 12 (1) (2019) 281–289.

[66] M. S. Zantye, A. Arora, M. M. F. Hasan, Operational power plant scheduling with flexible carbon capture: A multistage stochastic optimization approach, Computers & Chemical Engineering 130 (2019) 106544.

[67] M. S. Zantye, M. Li, M. M. F. Hasan, Optimal integration of renewables, flexible carbon capture, and energy storage for reducing CO_2 emissions from fossil power plants, in: Computer Aided Chemical Engineering, Vol. 50, Elsevier, 2021, pp. 1535–1540.

[68] D. S. Mallapragada, E. Gençer, P. Insinger, D. W. Keith, F. M. O'Sullivan, Can industrial-scale solar hydrogen supplied from commodity technologies be cost competitive by 2030?, Cell Reports Physical Science 1 (9) (2020) 100174.

[69] M. J. Economides, M. Aguirre, A. Morales, S. Naha, H. Tijani, L. Vargas, The economics of gas to liquids compared to liquefied natural gas, World Energy 8 (1) (2005) 136–140.

[70] Y. K. Salkuyeh, T. A. Adams II, Combining coal gasification, natural gas reforming, and external carbonless heat for efficient production of gasoline and diesel with CO_2 capture and sequestration, Energy Conversion and Management 74 (2013) 492–504.

[71] W. Zhang, J. Yang, Z. Zhang, J. D. Shackman, Natural gas price effects in china based on the CGE model, Journal of Cleaner Production 147 (2017) 497–505.

[72] B. Ali, Techno-economic optimization for the design of solar chimney power plants, Energy Conversion and Management 138 (2017) 461–473.

[73] I. D. Elyakova, A. A. Khristoforov, A. L. Elyakov, L. I. Danilova, T. A. Karataeva, E. V. Danilova, Forecast scenarios of world prices for natural gas (2017).

[74] S. Khajepour, M. Ameri, Techno-economic analysis of using three fresnel solar fields coupled to a thermal power plant for different cost of natural gas, Renewable Energy 146 (2020) 2243–2254.

[75] A. Elgowainy, K. Reddi, M. Mintz, D. Brown, H2A delivery scenario analysis model version 3.0*(HDSAM 3.0) user's manual (2015).